

Article

Design and Optimization of the Internal Geometry of a Nozzle for a Thin-Slab Continuous Casting Mold

Fernando S. Chiwo¹, Ana del Carmen Susunaga-Notario², José Antonio Betancourt-Cantera³, Raúl Pérez-Bustamante³, Víctor Hugo Mercado-Lemus³, Javier Méndez-Lozoya⁴, Gerardo Barrera-Cardiel⁵, John Edison García-Herrera⁶, Hugo Arcos-Gutiérrez^{6,*} and Isaiás E. Garduño^{6,*}

- ¹ CIATEQ A.C., Eje 126 No. 225, Zona Industrial del Potosí, San Luis Potosí 78395, Mexico; fernando.chiwo@ciateq.mx
- ² CONAHCYT—ICAT Instituto de Ciencias Aplicadas y Tecnología, Universidad Nacional Autónoma de México, Circuito Escolar s/n, Ciudad Universitaria, Col. UNAM, C.U., Delegación Coyoacán, Ciudad de México 04510, Mexico; ana.susunaga@icat.unam.mx
- ³ CONAHCYT—Corporación Mexicana de Investigación en Materiales (COMIMSA), Ciencia y Tecnología No. 790, Fraccionamiento Saltillo 400, Saltillo 25290, Mexico; jose.betancourt@ciateq.mx (J.A.B.-C.); raul.perez@ciateq.mx (R.P.-B.); victor.mercado@ciateq.mx (V.H.M.-L.)
- ⁴ Instituto Tecnológico de San Luis Potosí, Tecnológico s/n, Col. Unidad, Ponciano Arriaga, Soledad de Graciano Sánchez 78436, Mexico; javier.ml@slp.tecnm.mx
- ⁵ Instituto de Investigaciones Metalúrgicas, Universidad Michoacana de San Nicolás de Hidalgo, Morelia 58000, Mexico; gbarrera@umich.mx
- ⁶ CONAHCYT—CIATEQ A.C., Eje 126 No. 225, Zona Industrial del Potosí, San Luis Potosí 78395, Mexico; john.garcia@ciateq.mx
- * Correspondence: hugo.arcos@ciateq.mx (H.A.-G.); isaias.garduno@ciateq.mx (I.E.G.)



Citation: Chiwo, F.S.; Susunaga-Notario, A.d.C.; Betancourt-Cantera, J.A.; Pérez-Bustamante, R.; Mercado-Lemus, V.H.; Méndez-Lozoya, J.; Barrera-Cardiel, G.; García-Herrera, J.E.; Arcos-Gutiérrez, H.; Garduño, I.E. Design and Optimization of the Internal Geometry of a Nozzle for a Thin-Slab Continuous Casting Mold. *Designs* **2024**, *8*, 2. <https://doi.org/10.3390/designs8010002>

Received: 24 October 2023
Revised: 7 December 2023
Accepted: 18 December 2023
Published: 22 December 2023



Copyright: © 2023 by the authors. Licensee MDPI, Basel, Switzerland. This article is an open access article distributed under the terms and conditions of the Creative Commons Attribution (CC BY) license (<https://creativecommons.org/licenses/by/4.0/>).

Abstract: Understanding the phenomena that cause jet oscillations inside funnel-type thin-slab molds is essential for ensuring continuous liquid steel delivery, improving flow pattern control, and increasing plant productivity and the quality of the final product. This research aims to study the effect of the nozzle's internal design on the fluid dynamics of the nozzle-mold system, focusing on suppressing vorticity generation below the nozzle's tip. The optimized design of the nozzle forms the basis of the results obtained through numerical simulation. Mathematical modeling involves fundamental equations, the Reynolds Stress Model for turbulence, and the Multiphase Volume of Fluid model. The governing equations are discretized and solved using the implicit iterative-segregated method implemented in FLUENT®. The main results demonstrate the possibility of controlling jet oscillations even at high casting speeds and deep dives. The proposed modification in the internal geometry of the nozzle is considered capable of modifying the flow pattern inside the mold. The geometric changes correspond with 106% more elongation than the original nozzle; the change is considered 17% of an inverted trapezoidal shape. Furthermore, there was a 2.5 mm increase in the lower part of both ports to compensate for the inverted trapezoidal shape. The newly designed SEN successfully eliminated the issue of jet oscillations inside the mold by effectively preventing the intertwining of the flow. This improvement is a significant upgrade over the original design. At the microscale, a delicate force balance occurs at the tip of the nozzle's internal bifurcation, which is influenced by fluctuating speeds and ferrostatic pressure. Disrupting this force balance leads to increased oscillations, causing variations in the mass flow rate from one port to another. Consequently, the proposed nozzle optimization design effectively controls microscale fluctuations above this zone in conjunction with changes in flow speed, jet oscillation, and metal–slag interface instability.

Keywords: thin-slab mold; jet oscillations; nozzle optimization; numerical simulation

1. Introduction

Currently, there is an increasing worldwide need for steel. As a result, steel companies are facing strict market demands to enhance their products while maintaining high steel

quality. Thus, they have turned to thin-slab continuous casting in funnel-type molds, which has gained widespread acceptance, mainly due to the reduced slab thickness, faster casting speed, and fewer steps required to achieve the final product compared to casting in traditional slab molds.

However, it is possible to optimize the process; clearly, the distribution and variations in the speed of the exit ports of the submerged entry nozzle (SEN) determine the dynamic evolution of the flow pattern in the mold. Together with other process parameters (e.g., width and thickness of mold, depth of immersion of the nozzle, the flow control system and its design (stopper rod flow), the ports of the nozzle, and the internal geometry of the nozzle), this strongly affects the turbulent phenomena within the nozzle.

Consequently, the nozzle's interior geometric design is crucial for maximizing fluid flow in funnel-style continuous casting molds. By preventing operating faults that are dependent on the oscillation speed of the discharge jets originating from the nozzle ports and, consequently, the fluctuation of the interface, such a design is essential to enhancing the quality and cleanliness of cast steel [1,2]. In recent research, the flow of liquid steel was measured using a dye tracer, particle image velocimetry, and video recording tests utilizing a water-physical model of a funnel-type thin-slab mold fed by a two-port SEN [3,4]. Furthermore, the interaction of the swirling jets with the wide sidewalls of the mold causes asymmetrical flow inside the mold [5,6]. In molds with lower aspect ratios, where the jets do not touch the wide side walls, the flow pattern is symmetrical about the central plane [7].

Computationally and experimentally, thin-slab caster modeling requires extra attention due to many complexities that are typically not evident and important for standard slab caster modeling. These include the effects of liquid steel mass reduction due to solidification [8], shell formation, model bottom, and electromagnetic brake [9,10], and its effect on the level of fluctuation heights in the mold [11,12]. In this case, electromagnetic fields have emerged as powerful tools for addressing current problems in thin-slab continuous casting processes in the iron and steel industry [13]. In particular, the electromagnetic brake adopted a new magnet type specially designed for the thin-slab casting funnel-shaped mold [14]. Furthermore, authors like Wang et al. [15] studied predicting transient fields in the caster using a large eddy simulation and an enthalpy-porosity method; such a method helps predict the solidification shell in addition to increasing the possibility of washing the solidified steel crust [16] and possible wire breakage [17]. Also, there are other consequences to consider: slag trapping toward the sinus of liquid metal [18,19], slag droplets into steel volume [20], the movement of inclusions [13], and the possible reoxidation of the liquid steel due to the opening of the slag [21,22], as has been shown through numerical simulation techniques using colorimetry and PIV [23].

However, the developments of some works align with the research of mold flow patterns using mathematical simulation and physical modeling [24–26]. There are characteristics of this movement by eddies that vary in duration and length [27]. The biggest eddies are usually around the same magnitude as the mean flow's characteristic length. The minor scales dissipate the kinetic energy of the turbulence. In several of these works, the study of the asymmetries of the upper recirculation in the mold [28] proved that they strongly affect the meniscus shape [29] and depend directly on the fluctuations of the discharge jets [30,31]. Zhang et al. [32] showed both experimental and calculated results that the molten steel velocity near the mold surface increases with increasing casting speed. Additionally, the authors included argon gas injection that slowed down the molten steel velocity and uplifted the jet zone due to the buoyancy of bubbles.

In most works, modifying the nozzle enables better control and reduction of the oscillations of the jets [22,30]. Considering the above, another work [33] studied the effect of the nozzle internal design, focusing on the stability and oscillation of the jets. The findings indicate the origin of the oscillations inside the nozzle, mainly due to the change in pressure. Fluctuation at the tip of the port divider and the change in velocity in fluid layers above this zone generate an oscillating mass flow delivered in each nozzle port. The

increased phenomenology inside the mold corresponds to the vortex path formed below the tip of the nozzle. Therefore, it causes a continuous exchange of energy between jets due to the space generated by the geometry of the port divider [34].

Hence, in this study, we propose to optimize the design of the internal geometry of the nozzle. The improved design eliminates the space for the generation of the vortex path, eliminates the jet oscillation, and feeds the meniscus uniformly without causing fluctuations in the interface, even at high casting speeds.

2. Materials and Methods

2.1. Mathematical Modeling

The mathematical model studies the effect of optimizing the internal geometry of the nozzle ports on the dynamic pressure inside the nozzle, the vortex path generated below the nozzle tip, and the changes in the mass flow for a funnel-type thin-slab mold. The following subsection presents the different equations and models.

2.2. Fundamental Equations and Modelling Conditions

Problems involving fluid flow are hardly independent in materials processing operations. The main objective of material processing operations is to melt, solidify, or alter substances chemically, structurally, or in shape. However, since most of these materials are in a fluid state (vapor or liquid) during at least part of the processing sequence, the movement of the fluid plays a crucial role in several of these operations. Consequently, a better understanding of fluid mechanics has resulted in further advancements in materials processing technology. The general formulation of fluid flow problems is through the statements of the Navier–Stokes equations, constituted by the continuity or conservation of the mass equation, which is essentially a mass balance, and the equation of motion, which expresses a moment balance.

The molten steel flowing into the SEN is the most important premise for the model’s construction; in this scenario, the mold is subject to unstable isothermal circumstances and behaves Newtonian to maintain a constant viscosity. First, the solid surfaces were subjected to the casting speed, the inlet, and the outflow, which were characterized as velocity inlets ($u_{in} = 4 \text{ m/min}$; $u_{in} = 6 \text{ m/min}$; $u_{in} = 8 \text{ m/min}$) and non-slip boundary conditions. Since the flux layer had little bearing in this instance, the mold top’s pressure inlet condition was employed to mimic the effects of a system exposed to the atmosphere ($p = 101,325 \text{ Pa}$, $T = 273 \text{ K}$, with gravity acting in the direction of casting). The ensuing subsections will cover the casting parameters and physical characteristics used in the simulations (see Figure 1).

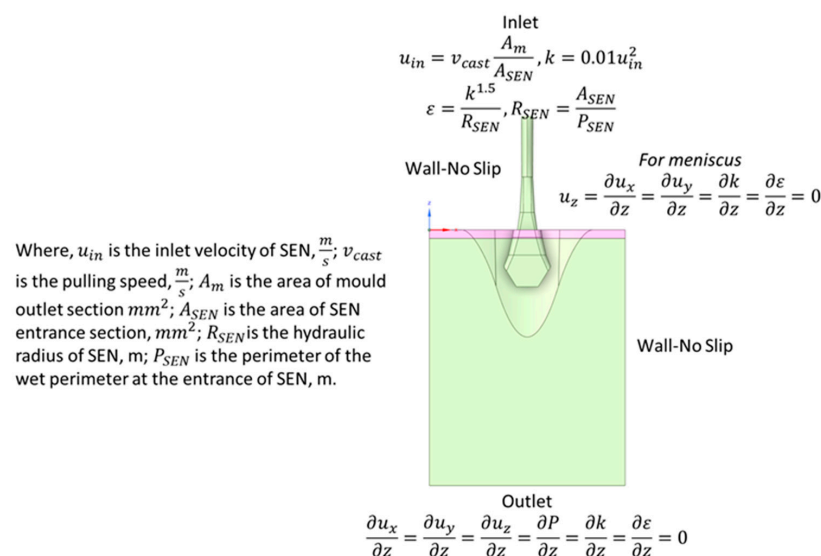


Figure 1. Boundary conditions for the thin-slab continuous casting mold.

After consideration, a brief description of the fundamental equations and the modelling conditions, the turbulence, and multiphase models in Cartesian coordinates are defined below.

The fundamental Navier–Stokes and continuity equations for incompressible fluid are as follows [35–37]:

$$\frac{\partial \rho}{\partial t} + \rho(\nabla u) = 0 \tag{1}$$

$$\rho \frac{\partial u}{\partial t} + \rho[u \cdot \nabla]u = -\nabla P + \mu_{eff} \nabla^2 u + \rho g \tag{2}$$

where t is the time; ρ is the fluid density; u represents the velocity; P and g represent the pressure and the gravity acceleration, respectively; and μ_{eff} , is the effective turbulent viscosity, to obtain the effective viscosity field; hence, μ_{eff} is the sum of the molecular viscosity μ and the turbulent viscosity μ_t .

It is a common practice to employ turbulence models that demand the inclusion of supplementary transport equations. These models lead to higher computational expenses and enhance the simulations' accuracy. In this case, the turbulence model k - ϵ standard is firstly used [38]:

$$\rho \frac{\partial k}{\partial t} + \rho \frac{\partial k u_i}{\partial x_i} = \frac{\partial}{\partial x_j} \left[\left(\mu + \frac{\mu_t}{\sigma_k} \right) \frac{\partial k}{\partial x_j} \right] + G_k - \rho \epsilon \tag{3}$$

$$\rho \frac{\partial \epsilon}{\partial t} + \rho \frac{\partial \epsilon u_i}{\partial x_i} = \frac{\partial}{\partial x_j} \left[\left(\mu + \frac{\mu_t}{\sigma_\epsilon} \right) \frac{\partial \epsilon}{\partial x_j} \right] + C_{1\epsilon} \frac{\epsilon}{k} G_k - C_{2\epsilon} \rho \frac{\epsilon^2}{k} \tag{4}$$

The model constants are $C_1 = 1.44$, $C_2 = 1.92$, $\sigma_k = 1.0$, $\sigma_\epsilon = 1.3$, and $C_\mu = 0.09$. G_k is the generation of turbulence kinetic energy owing to the mean velocity gradients, $G_k = \mu_t \frac{\partial u_j}{\partial x_i} \left(\frac{\partial u_i}{\partial x_j} + \frac{\partial u_j}{\partial x_i} \right)$.

Furthermore, the applied Reynolds Stress Model (RSM) [39,40] is defined as follows:

$$\begin{aligned} \frac{\partial}{\partial t} (\rho \langle U'_i U'_j \rangle) &= \frac{\partial}{\partial X_k} \left[\rho \langle U'_i U'_j U'_k \rangle + \langle P (\delta_{kj} U'_i + \delta_{jk} U'_i) \rangle \right] + \frac{\partial}{\partial X_k} \left[\mu \frac{\partial}{\partial X_k} \langle U'_i U'_j \rangle \right] \\ &\quad - \rho \left(\langle U'_i U'_j \rangle \frac{\partial U_j}{\partial X_k} + \langle U'_i U'_j \rangle \frac{\partial U_i}{\partial X_k} \right) - \rho \beta (g_i \langle U'_j \theta \rangle + g_j \langle U'_i \theta \rangle) \\ &\quad + \left\langle P \left(\frac{\partial U_i}{\partial X_j} + \frac{\partial U_j}{\partial X_i} \right) \right\rangle - 2\mu \left\langle \frac{\partial U_i}{\partial X_k} + \frac{\partial U_j}{\partial X_k} \right\rangle \\ &\quad - 2\rho \Omega_k \left(\langle U'_j U'_m \rangle \epsilon_{ikn} + \langle U'_i U'_m \rangle \epsilon_{jkn} \right) \end{aligned} \tag{5}$$

Moreover, a volume of fluid model was employed to solve the two-phase air–steel system. This model uses a tracking scheme design for two or more immiscible phases, where the interphase is between the fluids. This model has been widely employed in previous works and is fully described in the literature [5,33,36].

2.3. Multiphase Model

The volume of fluid (VOF) model is a tracking technology used for multiple phases of fluids that do not mix. The model focuses on determining the position of the interface between the fluids. The model uses a single momentum equation for the fluids, and a new variable is introduced for each additional phase, helping to calculate the physical properties of each phase based on its fraction of the total volume. The variables and properties are shared across all phases and represent the volume-averaged values. The fraction of each computational cell is traced across the domain to ensure it adds up to unity. In mathematical notation, if the q th-volume fraction in the cell is α_q , three conditions are possible.

- $\alpha_q = 0$ —the cell is empty (the q th phase is not present);
- $\alpha_q = 1$ —the cell is complete (it only contains the q th phase);

- $0 < \alpha_q < 1$ —the cell contains the interface between the q-th phase and one or more different phases.

2.4. Volume Fraction Equation

The location of the interface(s) between the phases themselves is accompanied by the solution of a continuity equation for the volume fraction of one (or more) of the phases. For the qth phase, the equation has the following form:

$$\frac{\partial \alpha_q}{\partial t} + \bar{v} \cdot \nabla \alpha_q = \frac{S_{\alpha_q}}{\rho_q} \tag{6}$$

The volume fraction equation will not be solved for the primary phase since the fraction is calculated based on the following:

$$\sum_{q=1} \alpha_q = 1 \tag{7}$$

The presence of the component phases of each control volume determines the properties that appear in the transport equations. For example, for a two-phase system, the phases are represented by subscripts 1 and 2, and if the volume fraction of the second phase is being tracked, the density in each cell is given by the following:

$$\begin{aligned} \rho &= \alpha_2 \rho_2 + (1 - \alpha_2) \rho_1 \\ \mu &= \alpha_2 \mu_2 + (1 - \alpha_2) \mu_1 \end{aligned} \tag{8}$$

2.5. Momentum Equation

Similarly, a single momentum equation is solved along the domain, and the resulting velocity field is shared between the phases. The momentum equation depends on each phase’s volume fraction through the properties ρ and μ .

$$\frac{\partial}{\partial t} (\rho \vec{v}) - \nabla \cdot (\rho \vec{v} \vec{v}) = -\nabla P + \nabla \cdot \left[\mu \left(\nabla \vec{v} + \nabla \vec{v}^T \right) \right] + \rho \vec{g} + \vec{F} \tag{9}$$

where the terms on the right are the pressure forces on the fluid; the viscous forces; the effective viscosity ($\mu_{eff} = \mu_L + \mu_T$), which represents the sum of the laminar and turbulent viscosity in the fluid during shear stresses; the effect of the force of gravity on the fluid; and the body forces represented by the vector \vec{F} , respectively. The term \vec{v}^T represents the time-averaged velocity vector.

2.6. Surface Tension

Surface tension is a result of the cohesive forces among fluid molecules. It refers to the Gibbs free energy required to alter the surface of a system under constant temperature, pressure, and composition. Surface tension plays a crucial role in balancing the attractive intermolecular forces against the external pressure gradient at the surface.

In regions where two fluids are separated, surface tension minimizes free energy by reducing the interface area. The surface tension model used is known as the continuum surface force (CSF) proposed by Brackbill. With this model, adding surface tension to the VOF model calculation results in a source term in the momentum equation.

To understand the origin of this source term, one can consider the case where the stress is constant along the surface, and only the forces normal to the interface are considered. It can be shown that the pressure drop along the surface depends on the coefficient of surface tension (σ), and the curvature of the surface is measured by two radii in orthogonal directions R_1 and R_2 .

$$P_2 - P_1 = \sigma \left(\frac{1}{R_1} + \frac{1}{R_2} \right) \tag{10}$$

P_1 and P_2 are the pressures in the two fluids on each interface side.

In the case of the CSF model, the curvature is calculated from the local gradients on the surface normal to the interface. Letting n be the surface normal, defined as the gradient α_q of in the q th phase, then

$$n = \nabla \alpha_q \tag{11}$$

The curvature (k) is defined in terms of the divergence from the unit normal:

$$k = \nabla \cdot \hat{n} \tag{12}$$

where

$$\hat{n} = \frac{n}{|n|} \tag{13}$$

when discussing surface tension, it is expected that reference is made to the pressure changes across a surface. The divergence theorem, which expresses the force acting on the surface, is used to calculate a volume force. This source term volume force is then incorporated into the momentum equation. By doing so, the equation can accurately calculate the force produced by surface tension.

$$F_{vol} = \sum_{ij,i < j} \sigma_{ij} \frac{\alpha_i \rho_i k_j \nabla \alpha_j + \alpha_j \rho_j k_i \nabla \alpha_i}{\frac{1}{2}(\rho_i + \rho_j)} \tag{14}$$

First, the numerical model runs for 60 s using the $k-\epsilon$ turbulence model to optimize the computational time and reach a faster convergence. Then, it is replaced by the RSM model in the simulation for another 300 s to accomplish a steady-state condition.

Using a first upwind strategy, the implicit segregated-iterative method yields the governing discretized equations as a first approach. Next, the SIMPLEC algorithm was considered for pressure–velocity coupling, and the body force weight was employed for pressure interpolation. Eventually, the convergence criterion was established when the total of the residuals was equal to or less than 10^{-4} . The mold thickness and width were constant for all studied cases; two simulated SEN immersions were used for five different casting speeds. After this, a modified SEN was created using the same simulated points and this newly proposed geometry. The physical properties of the fluid are illustrated in Table 1.

Table 1. Material properties [41,42].

Phase	Property	Value
Air	Density	1.225 kg/m ³
	Viscosity	1.7894 × 10 ⁻⁵ kg/m·s
Steel	Density	6971.4 kg/m ³
	Viscosity	6.4 × 10 ⁻³ kg/m·s
Air–Steel	Surface tension	1.6 N/m

Figure 2 schematically shows the essential geometry parameters for the funnel thin-slab mold and the two SENs studied. Figure 2f shows that the SEN internal modification increases the port’s internal bifurcation tip height. The computational domain consisted of 1,573,692 unstructured cells (336,716 nodes), as shown in Figure 3.

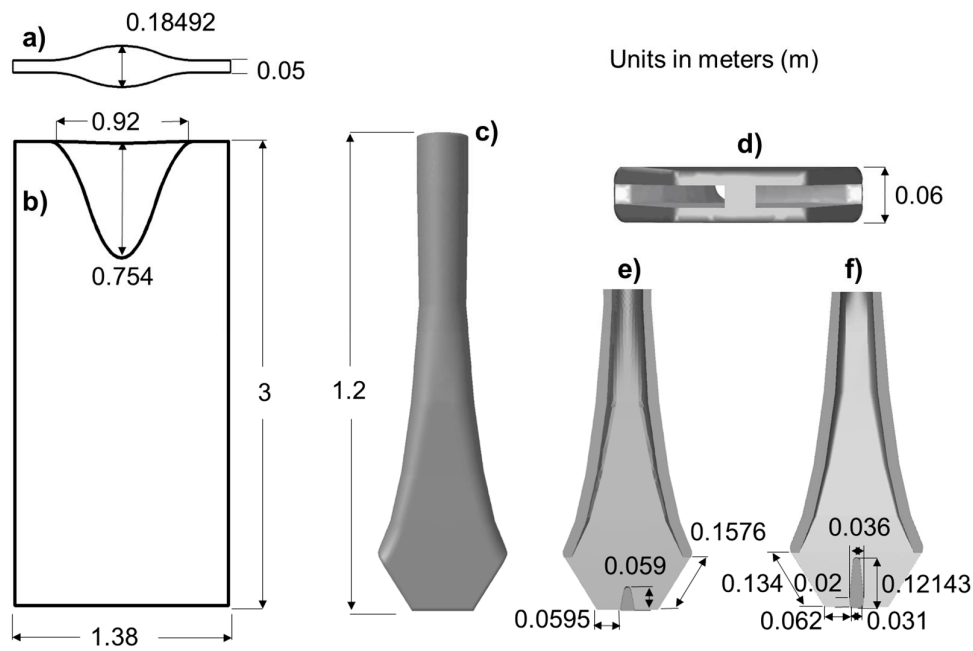


Figure 2. Schematic geometries for (a,b) the funnel thin-slab mold, (c,d) length and width dimensions of the SEN, (e) internal SEN—original, and (f) internal SEN—optimized.

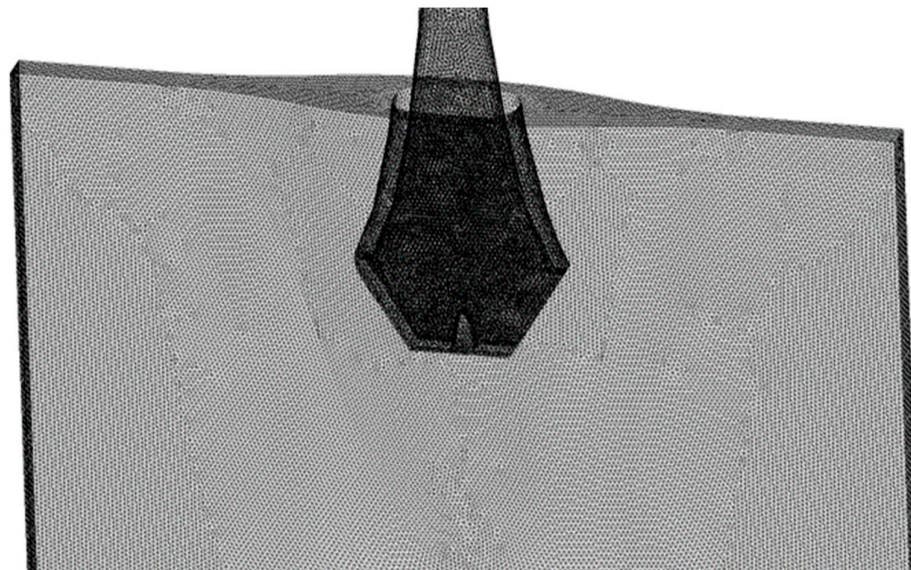


Figure 3. Mesh for the thin-slab continuous casting mold 3D model, scale 1:1. The mesh comprised 1,573,692 unstructured cells and 336,716 nodes.

3. Results

3.1. Analysis and Discussion of Results

This section provides an analysis and discussion of the results obtained for a nozzle currently used in industry and the optimized nozzle. This study contrasts the velocity vectors, velocity measurement, dynamic pressure contours, kinetic energy production, turbulent dissipation ratio, turbulent intensity, and magnitude of the vortex. Finally, a more precise understanding of the effect of each of these variables is presented. Here, the purpose is to analyze the jets' stability from the nozzle ports and the effect on the flow patterns generated inside the mold and the nozzle. The performed numerical experiments were carried out at 22 cm and 34 cm nozzle immersions and casting speeds of 4, 6, and 8 m/min.

3.2. Effect of the Internal Geometry of the Nozzle on Fluid Flow Phenomena Presented Inside the Mold

In previous works [5,21], the formation of dynamic distortions (DDs) in molds for thin slabs has been suggested to be a consequence of the imbalance in the turbulent kinetic energy balance and its production, mainly in the area located in the lower part of the nozzle. In these works, the analysis of DD as well as this hypothesis, which remains unproven, have been raised. Others [33] suggest that the DD starts from inside the nozzle, since the nozzle must deliver the flow to each port in a balanced fashion. Thus, we propose the hypothesis that feeding with fluctuations in each port favors the formation of DDs with different intensities.

This research work presents a new idea that contradicts previous ones. According to the findings, the origin of the DD is located inside the nozzle, specifically in the area above the divider of the ports where there are fluctuations in pressure and speed. This area suppresses the fluid below the nozzle tip, where the vortices that separate the boundary layer originate. This phenomenon and the vortex coming from the bottom of the mold cause the jets to lack symmetry and subsequent oscillation, especially at high casting speeds and immersion. The verification of this hypothesis is through a nozzle with a stable operation. The results for an optimized nozzle were compared with the results obtained with the original nozzle; the experiments were performed with two different depths of immersion and different casting speeds, from which the formation of DD was very likely.

Figure 4 shows the velocity profiles calculated at the center of the mold in a longitudinal plane for the three casting speeds selected at 22 cm immersion. Here, the flow patterns are characteristic of this mold, showing the formation of a significant recirculation on each side of the nozzle. Other important characteristics are the low-speed zones located at the corners in the mold's upper part, along the nozzle's vicinity, and the area below the nozzle between the two jets. A particular consideration, as shown in Figure 4a, is that the stability of the jets at a speed of 4 m/min is excellent for the original nozzle. However, the jets vary their flow pattern as the casting speed increases. For example, the observed variation in the jet on the left side (marked with the number 1) presents a more intense penetration than on the right side. This variation appears at a 6 m/min speed and is maintained up to the maximum 8 m/min rate.

In this part, a proposed modification in the internal geometry of the nozzle is considered (see Figure 4b), capable of modifying the flow pattern inside the mold. The conversion resulted in the ports being 106% more elongated than the original nozzle; the change also resulted in 17% of an inverted trapezoidal shape. Furthermore, there was a 2.5 mm increase in the lower part of both ports to compensate for the inverted trapezoidal shape. The current objective is to remove the area underneath the nozzle tip where dynamic distortion occurs, resulting in the nozzle's outgoing jets sharing their energy, thereby creating equilibrium between them. Consequently, the external effects of ferrostatic pressure and oscillations will be eliminated.

Regarding the flow patterns for a 22 cm nozzle immersion presented in Figure 4b, particularly the area marked with the number 1, the vectors move toward the flow of the jets. Thus, it is possible to invert the direction of the vectors to avoid the recirculating fluid coming from the bottom of the mold reaching the tip of the nozzle. The purpose is to eliminate the formation of the vortex path caused by the unstable separation of the boundary layer with the port divider, as happens with the original nozzle. This phenomenon is because the internal geometry directs the flow from the ports toward the center of the mold, thus sharing its energy until the momentum transport with the surrounding molten steel causes separation and joining with the lower and upper recirculation of the mold. In addition, the flow pattern is composed of two recirculations in the upper part of the mold and two in the lower part, as with the original nozzle; however, unlike the original, it has good symmetry in the behavior of the jets coming from the nozzle at different speeds.

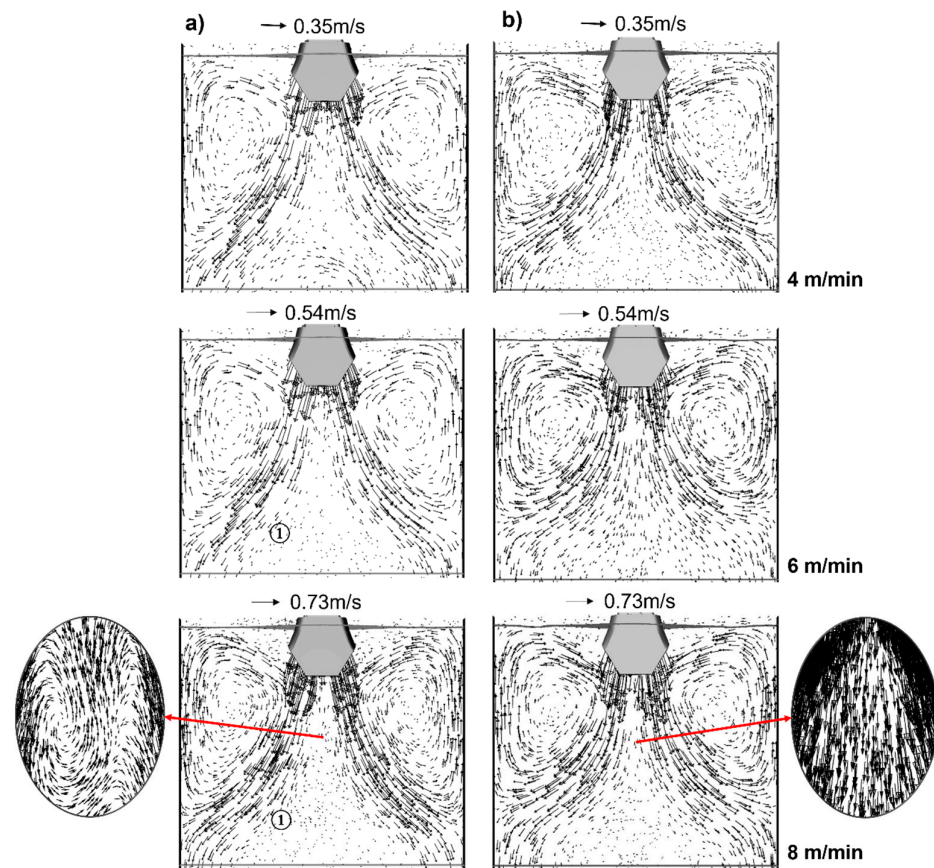


Figure 4. Velocity vectors in the central symmetrical plane of the 22 cm nozzle immersion mold: (a) original nozzle; (b) optimized nozzle.

An approach to verify the aforementioned is performed in the flow region between the two jets. In that zone for the original nozzle (left side, Figure 4a, 8 m/min), vorticity formation is due to the detachment of the boundary layer of the port divider. Consequently, the vorticity increases due to the gain of kinetic energy from the jet. Also, an observed dissolution of this vorticity occurs when it collides with another vorticity coming from the bottom. For the optimized nozzle (right side, Figure 4b, 8 m/min), the region for the formation of vortices showed suppression due to the detachment of the boundary layer. In this region, the jets share energy, provoking the flow to move to the bottom of the mold. Therefore, reducing the kinetic energy transfer and vorticity dissipation keeps the jets symmetrical.

The nozzle is placed in 34 cm immersion (see Figure 5), which presents the typical pattern of thin-slab flows. However, as the casting speed increases, the jets begin to oscillate. Figure 5a shows the most significant deviation on the left jet (speed 6 m/min, point 1), and on some occasions, the jet on the right side, as shown in Figure 5a, at a speed of 8 m/min. The proposed study was deeper, considering the immersion depths of the nozzles, the different casting speeds, and the space between the jets. Thus, it can be seen that the space between the two jets at both nozzle immersion depths and the different casting speeds is used so that there is an exchange of energy between the vorticity generated due to the separation of the boundary layer in the divider of the ports and the vorticity coming from the recirculation from the bottom of the mold. Hence, the vorticity is due to the separation of the boundary layer in the port divider. In the case of the optimized nozzle in Figure 5b, the jets maintain good symmetry in the three speeds analyzed because of the flow direction caused by the optimization of the division of the ports of this nozzle. This avoids the formation of vorticity caused by the detachment of the boundary layer of the port divider towards the mold, and the effects of vorticity coming from the bottom of the mold will hardly affect the stability of the jets from the nozzle ports.

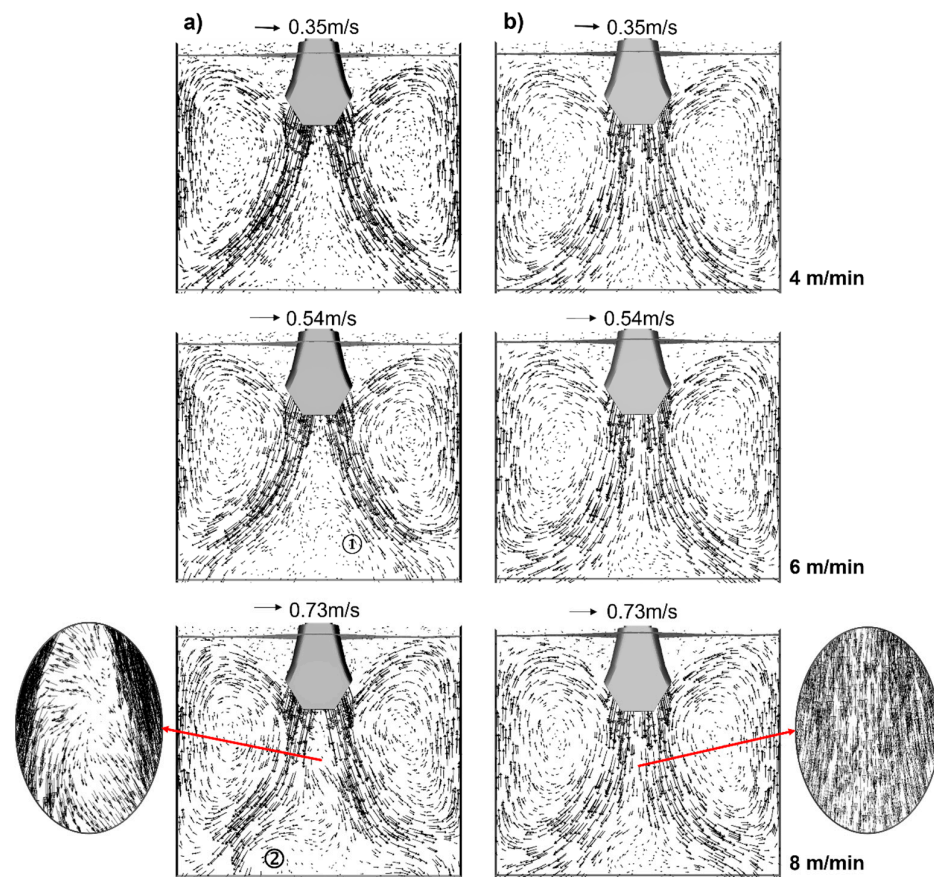


Figure 5. Velocity vectors in the central symmetrical plane of the cast at a nozzle immersion of 34 cm: (a) original nozzle; (b) optimized nozzle.

In the same way, for the 22 cm nozzle immersion, the approach is in the flow region between the two jets. In this case, for the 34 cm nozzle immersion, for the original nozzle (left side, Figure 5a, 8 m/min) the formation of vorticity of high energy intensity is due to energy exchange between the jets and the vortices. The mechanism described is generated by separating the boundary layer of the division of ports. Additionally, vorticity from the recirculation of the mold bottom causes continuous oscillation of the jets. For the optimized nozzle (right side Figure 5b, 8 m/min), the energetic phenomenon and, therefore, the vortex path was eliminated, thus obtaining well-defined jets without oscillating periods.

Inside the mold, speed variations of the fluid exist due to fluctuations in the oscillation of the jets. All these effects have a direct impact on the behavior of the meniscus. This methodology draws a line from the center to the thin left and right walls if the observed oscillations affect the meniscus. The applied method resulted in depths of 43 to 22 cm and 55 cm to 34 cm and the corresponding fluid velocities.

In Figure 6, showing the 22 cm nozzle immersion, the area marked with the number (1) corresponds to the area just below the tip of the nozzle, and the original nozzle has a lower speed than the modified nozzle. Such behavior is related to the more significant separation of the jets and the direction of the fluid. Since the original nozzle allows the fluid from the bottom recirculation to touch the nozzle tip, the modified nozzle presents a higher speed in this area. Evidence shows increments in the instability of this area and the continuous formation of a vortex path. On the other hand, the impact of both jets causes higher speeds in this area. Thus, reducing the separation causes the fluid from the bottom to reach the nozzle tip.

Furthermore, in zone 2, unlike the 22 cm immersion, the speed between the two nozzles is almost the same for the three different casting speeds. In contrast, zone 3 at 22 cm remains in the center of the superior recirculation, where the velocity for both nozzles is

very close to zero. Finally, in zone (4) for 34 cm immersion, the original nozzle presents an oscillating behavior of the jets for 4, 6, and 8 m/min, increasing its intensity with casting speed. Therefore, this behavior results from the continuous fluctuation of the meniscus and the unstable and fluctuating interface.

The proposed methodology considers drawing two lines at 7 mm height from the left side of the nozzle to the right side of the mold below the interface to check the stability of the interface (air–steel). Both nozzles and immersions used the methodology to measure the current velocities in that area (see Figure 8).

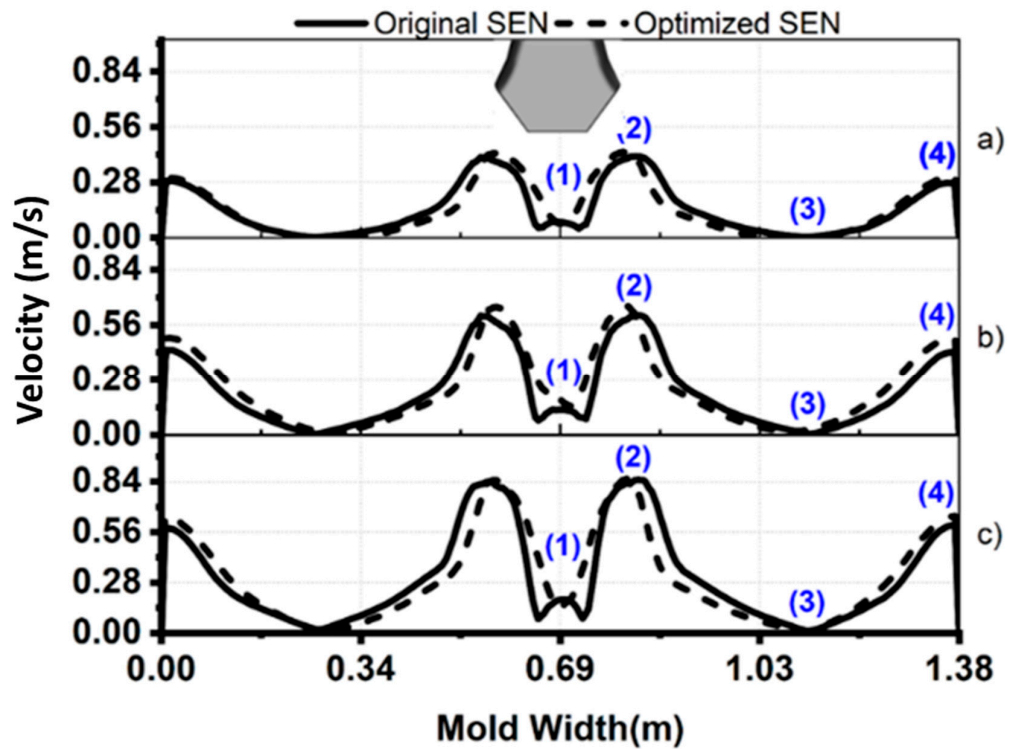


Figure 6. Velocity vs. mold width for 22 cm immersion contrasted for original SEN and optimized SEN. (a) Casting speed 4 m/min, (b) Casting speed 6 m/min, (c) Casting speed 8 m/min.

Now, the attention goes to zone 2, where the velocity of the jets for both nozzles is of interest. In this consideration, the velocity of the jets is slightly higher for the modified nozzle at 4 and 6 m/min parts (a) and (b), while for 8 m/min, it is the same for both subjects. In the case of zone 3, there are no significant changes between both nozzles, and the fluid velocity is very close to zero because it is in the center of the upper recirculation of the mold. Finally, regarding the area near the thin wall of the mold (4), at 4 m/min, both nozzles have the same behavior, and there is symmetry in their speed, while for 6 and 8 m/min, parts (b) and (c), there is a slightly higher speed for the modified nozzle. Here, there is already a slight oscillation in the original nozzle. The rate on both walls differs, reflecting the lack of homogeneity in feeding the meniscus. Concerning the 34 cm nozzle immersion in Figure 7, the separation of the jets is even greater between both nozzles. The original nozzle for 22 cm also continues to present the same behavior. In contrast, the modified nozzle increases the speed in this area, thus eliminating the appearance of the vortex path allowed by the original nozzle.

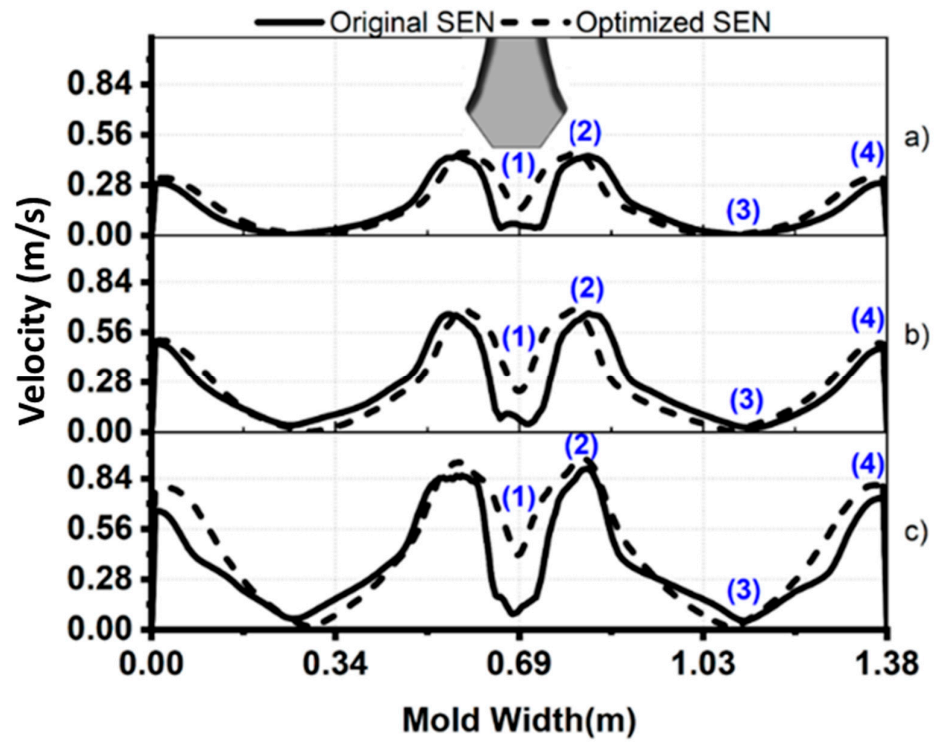


Figure 7. Velocity vs. mold width for 34 cm immersion contrasted for original and optimized SEN. (a) Casting speed 4 m/min, (b) Casting speed 6 m/min, (c) Casting speed 8 m/min.

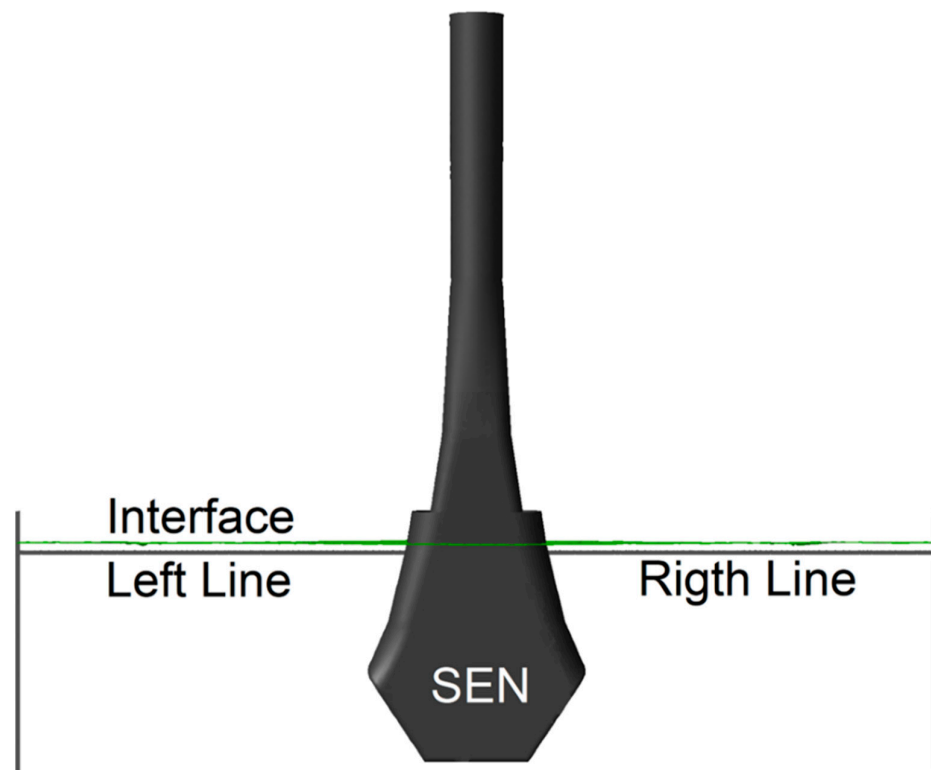


Figure 8. Diagram of the positions of the measurements inside the mold. The velocity measurements are made below the air–steel interface on the right and left sides of the SEN.

In Figure 9, for 22 cm nozzle immersion and the different casting speeds, the results show that the optimized nozzle feeds the meniscus better and in a more homogeneous

way, contrary to the original nozzle. This situation is a consequence of the symmetry of the jets and the existing stability; since there are no oscillations, the behavior does not cause instability in the interface or fluctuations.

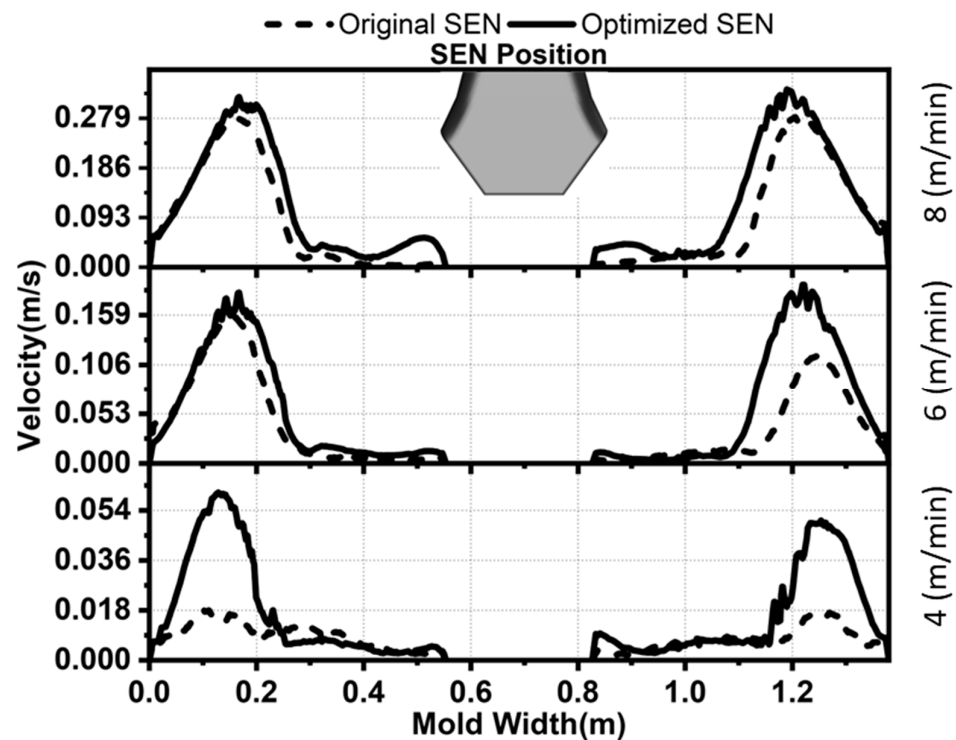


Figure 9. Effect of the geometry of the nozzle ports’ internal division on the fluid’s velocity below the air–steel interface at a nozzle immersion of 22 cm for casting speeds of 4 m/min, 6 m/min, and 8 m/min.

Figure 10 shows the 34 cm nozzle immersion depth. The optimized nozzle offers better feeding and homogeneity to the meniscus than the original nozzle because of the more intense oscillation of the jets coming from the original nozzle. The pressure and velocity fluctuations inside this nozzle are more intense than this oscillating phenomenon and cause the instability of the interface. The results presented so far verify that the DD originates inside the nozzle. In the case of discharge oscillation, jets occur due to vortex exchange in the space generated between them (original nozzle). Based on the results presented so far, the next step was to conduct a more detailed analysis of the mathematical simulation within the SEN using dynamic pressure contours. For this, the most relevant casting speeds were selected: lowest, medium, and highest (4 m/min, 6 m/min and 8 m/min).

The analysis through velocity vectors helps to understand the effect on generating and suppressing vorticity formation. Regardless, this analysis does not entirely clarify the impact of the optimization of the nozzle geometry over the origin of vorticity and the jets’ oscillations. Therefore, it is necessary to determine dynamic pressure contours in a plane longitudinal to the center of the nozzle at different times for each case. In addition, each discharge jet monitors the delivered mass flows. Figures 11–13 show the information on the topics mentioned.

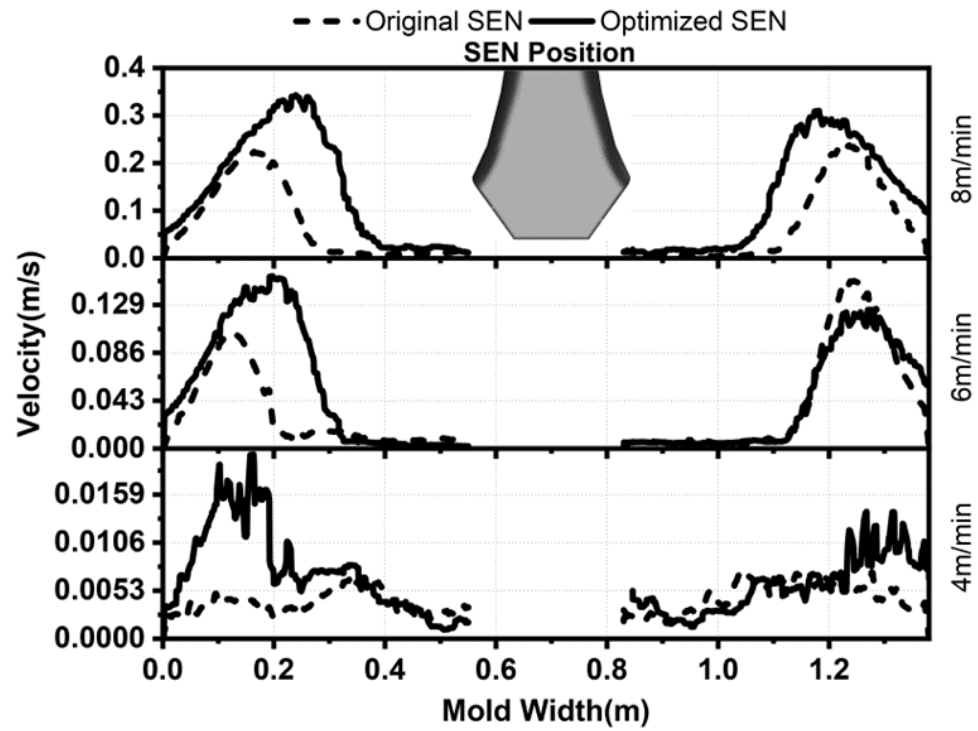


Figure 10. Effect of the geometry of the nozzle ports' internal division on the fluid's velocity below the air–steel interface at a nozzle immersion of 34 cm for casting speeds of 4 m/min, 6 m/min, and 8 m/min.

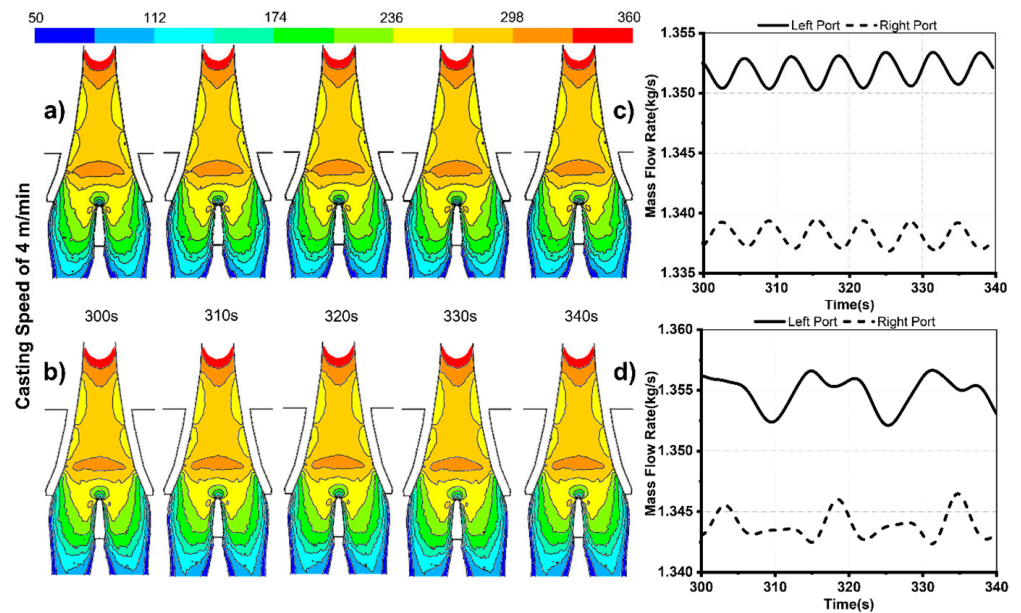


Figure 11. Dynamic pressure contour (Pa) in a central symmetrical original nozzle at a 4 m/min casting speed and mass flow monitoring for each port. (a,c) 22 cm immersion; (b,d) 34 cm immersion.

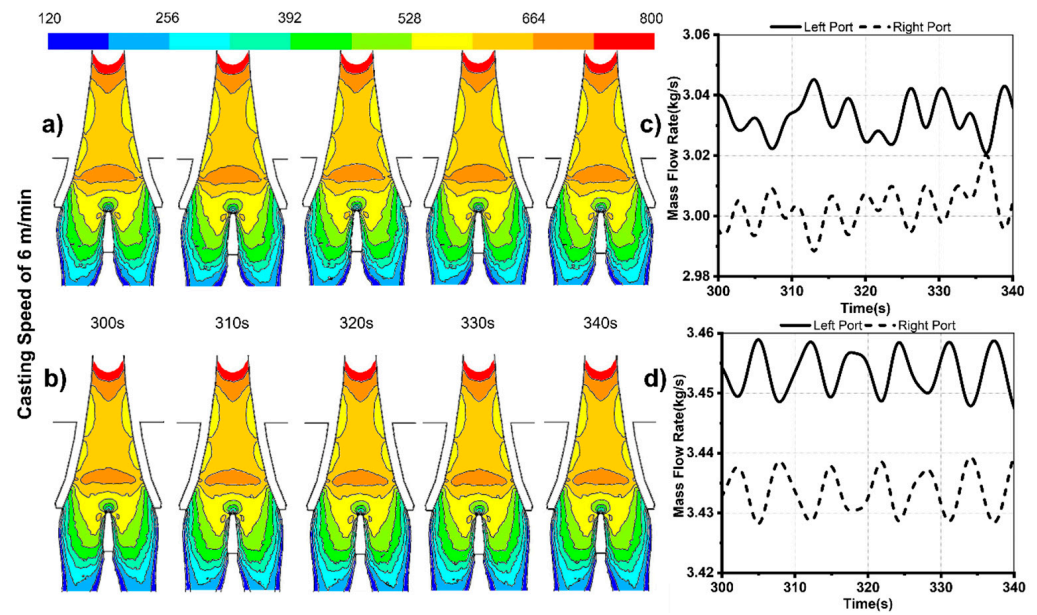


Figure 12. Dynamic pressure contour (Pa) in a central symmetrical original nozzle at 6 m/min casting speed and mass flow monitoring for each port. (a,c) 22 cm immersion; (b,d) 34 cm immersion.

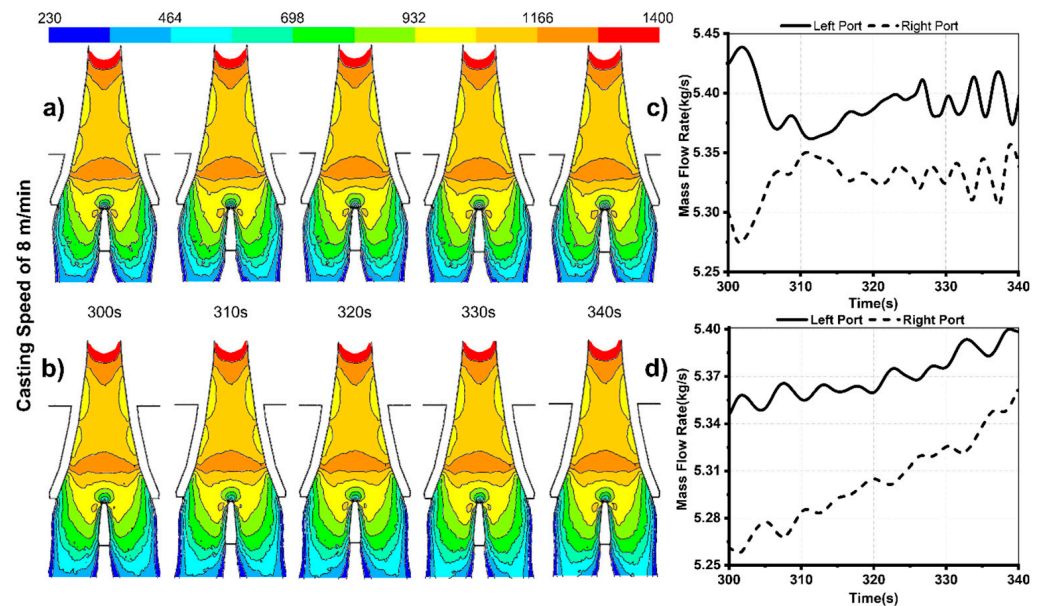


Figure 13. Dynamic pressure contour (Pa) in a central symmetrical original nozzle at an 8 m/min casting speed and mass flow monitoring for each port. (a,c) 22 cm immersion; (b,d) 34 cm immersion.

The design of the original nozzle shows a variation in the change in its geometry. However, the differences are produced gradually (common in nozzles for thin slabs), indicating no restriction over the flow development in its interior due to a considerable imbalance of forces. Thus, the pressure contours show this is not the case, and the changes do not represent any effect. When examining the first two changes inside the nozzle (specifically, the increases in the area at points 1 and 2 in Figure 11), it becomes clear that they gradually impact the flow development and the formation of low-pressure areas (known as vein contraction), suggesting that the fluid does not completely detach from the boundary layer. However, the feed rate makes it difficult to track the geometric changes.

These variations hold their position regardless of whether the nozzle is at 22 or 34 cm immersion and whether the casting speed increases. However, as the casting speed in-

creases, these zones decrease slightly in size, as shown in Figures 11–13. After going through the first two area changes, the fluid shows certain variations, since the low-pressure zones are not symmetrical, indicating initial fluctuations in flow patterns. As the fluid decreases, it enters the third change in the area (Figure 11). In the area under analysis, the low-pressure regions on the sides of the nozzle disappear. Accordingly, there is an increase in pressure across the entire width due to a decrease in the area. The fluid exiting shows a clear imbalance at the top of the port, and its tendency toward the left port is evident for both dives when operating at casting speeds of 4 and 6 m/min.

As the casting speed increases, the higher-pressure zone tends to enlarge. As a result, the tendency of the fluid toward the ports is now variable (Figure 13). Shape variations in the shape of the interior of the nozzle generate disturbances in the fluid. Hence, the tendency is to exit through a port preferentially. However, despite these observed variations, there is no evident phenomenon for the jets to present more significant oscillations and generate the formation of DDs.

The analysis continues, following the trajectory of the fluid as it impacts the port divider (triangular shape located in the lower part of the nozzle). At this point, there is again a more intense variation in dynamic pressure. Figure 11 shows this, at a casting speed of 4 m/min and in the position of 22 cm, with Figure 11a showing the variations in pressure in the said zone that do not change with time. However, as the nozzle passed 34 cm immersion, the dynamic pressure at the tip of the triangle showed small fluctuations concerning time; see Figure 11b. Therefore, the mass flow was determined as a function of time to determine whether these variations affected the jet oscillation, as shown in Figure 11c,d.

The elements discussed above are confirmed at a 22 cm immersion position, since observations showed that the fluid has a clear and constant tendency to exit through the left port. However, at 34 cm immersion, the variations observed at the tip of the mentioned triangle generate that the mass flow in each jet to oscillate, showing that the flow through the left side port periodically decreases and increases by the same magnitude as the right side port. When increasing the casting speed to 6 m/min, Figure 12 shows that at 22 cm of nozzle immersion, the zone of dynamic pressure variation on the tip of the triangle remains constant and that the fluid has the same tendency to exit more through the left port; see Figure 12a,c. At this same speed, at 34 cm immersion of the nozzle, the variations in dynamic pressure at the triangle tip become more evident. Figure 12b,d shows the jets' effects on the oscillations. In the case of a casting speed of 8 m/min, variations on the triangle tip appear even from at 22 cm immersion, as seen in Figure 13a,c, and 34 cm immersion of the nozzle results in a higher oscillation frequency.

4. Discussion

4.1. Optimized Nozzle

Optimizing the internal geometry eliminates the area below the nozzle's tip where a vortex path originates, raising the dynamic distortion and forcing the jets [33]. In addition, the projections of the nozzle share their energy to create a balance between both, eliminating the external effect of ferrostatic pressure and oscillations.

4.2. Analysis Inside the Optimized Nozzle

Figures 14–16 show the dynamic pressure contours in a longitudinal plane to the center of the nozzle. The results show that points 1 and 2 are similar to those of the original nozzle. In contrast, there are notable differences between the two nozzles, with a more significant increase in dynamic pressure for the optimized nozzle than that presented by the original nozzle. This phenomenon causes a fluctuation in pressure and the fluctuating velocity caused by the fluid jet impact on the nozzle point to have a minor effect on the inhomogeneity in the movement transfer in fluid zones above this area, as reported previously in the literature [4,5].

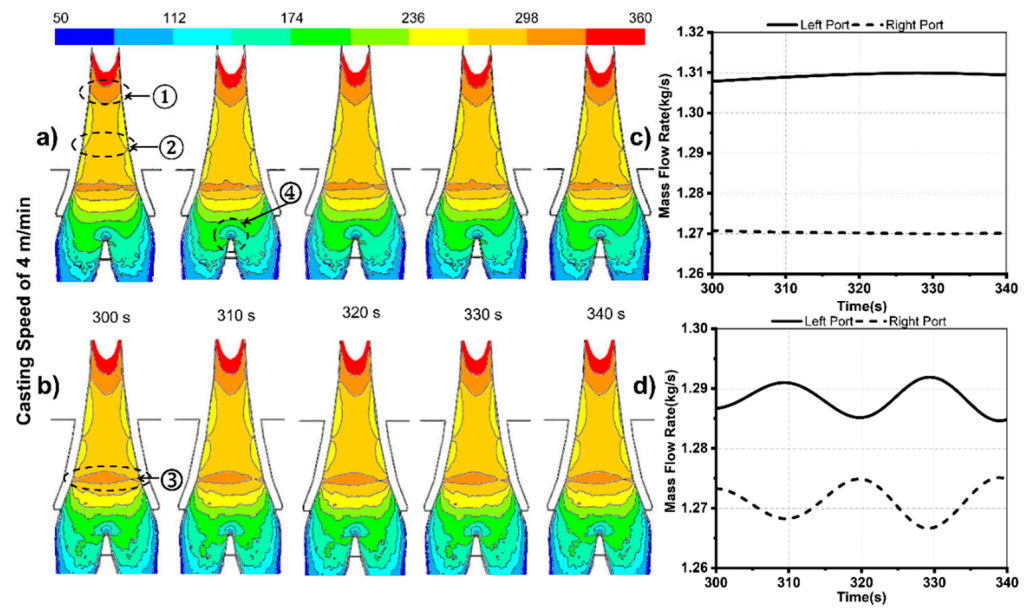


Figure 14. Dynamic pressure contour (Pa) in a central symmetrical plane of the optimized nozzle at a casting speed of 4 m/min and mass flow monitoring for each port (a,c) at 22 cm nozzle immersion and (b,d) at 34 cm nozzle immersion.

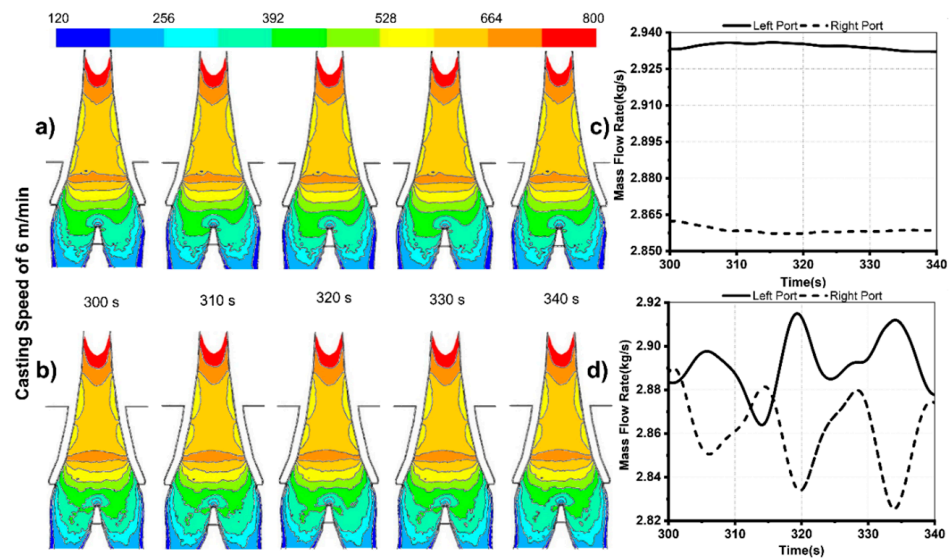


Figure 15. Dynamic pressure contour (Pa) in a central symmetrical plane of the optimized nozzle at a casting speed of 6 m/min and mass flow monitoring for each port (a,c) at 22 cm nozzle immersion and (b,d) at 34 cm nozzle immersion.

When comparing the observed point to the original nozzle, it is evident that it has a more stable area, with less significant geometry changes confirmed by observing each port’s mass flow behavior. As a result, this nozzle experiences less variation and maintains consistent flow through only one port, preventing entanglements and oscillations in the jet’s behavior, as seen in the original nozzle.

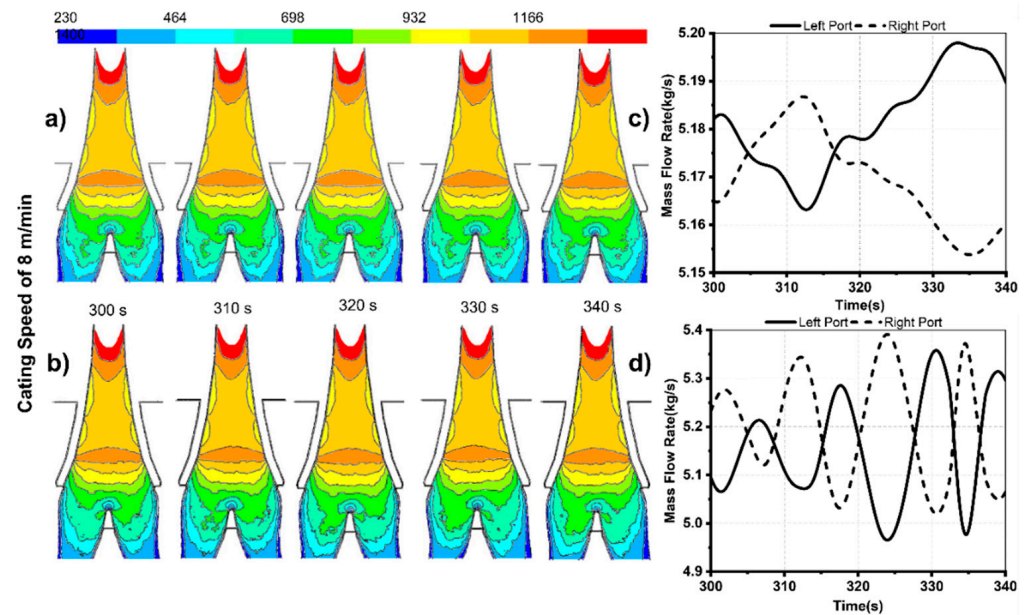


Figure 16. Dynamic pressure contour (Pa) in a central symmetrical plane of the optimized nozzle at a casting speed of 8 m/min and mass flow monitoring for each port (a,c) at 22 cm nozzle immersion and (b,d) at 34 cm nozzle immersion.

4.3. Analysis Inside the Nozzle-Mold System

The geometry of the nozzle has a determining influence on the flow within the mold [23,30]. However, comparing the numerical models shows that the outlet flow changes depending on the nozzle’s specific geometric characteristics, such as its length, metallurgical height, and the size and shape of the outlet ports. In addition, some of these characteristics change naturally due to continuous casting operating conditions. The most straightforward example is the port’s geometry modification due to the nozzle’s wear caused by the erosion and deposition of impurities. Therefore, to correctly characterize the flow behavior within the nozzle, it is necessary to reproduce the conditions at different operating regimes and determine the effect of the initial geometric design conditions.

Consequently, an in-depth analysis of the original nozzle and an optimized one was carried out. The analysis was done by drawing a straight line in the center of the interior of the nozzle and the mold, from which the production of kinetic energy was obtained as well as the relationship of turbulent dissipation, turbulent intensity, and vorticity magnitude. By doing this, we have a more precise understanding of the effect of each of these variables on the stability of the jets coming from the nozzle ports and their effect on the flow patterns generated inside the mold and the nozzle. Each of the variables mentioned above was measured for 22 cm and 34 cm nozzle immersions and casting speeds of 4, 6, and 8 m/min.

In Figure 17a for a 22 cm immersion, as the speed changes from 4 to 5 m/min, the turbulent kinetic energy does so in tandem, starting with a large generation of turbulent kinetic energy in that region; the energy of the original nozzle is slightly more significant than that of the optimized nozzle. Now, as seen in Figure 17a, for an 8 m/min casting speed, a considerable difference is seen between the two nozzles, since the turbulent kinetic energy for the original nozzle is very close to zero. As a result, the fluid’s behavior inside this nozzle is almost laminar, until it reaches the tip of the division of the ports where the original nozzle remains, which generates more kinetic energy in this area.

On the other hand, looking inside the mold, an area with a more significant generation of turbulent kinetic energy is from the tip of the nozzle to 32 cm below it; for this reason, the original nozzle reaches a value slightly higher than that of the optimized nozzle. After that, however, gradual energy decay occurs, until it reaches a value very close to zero.

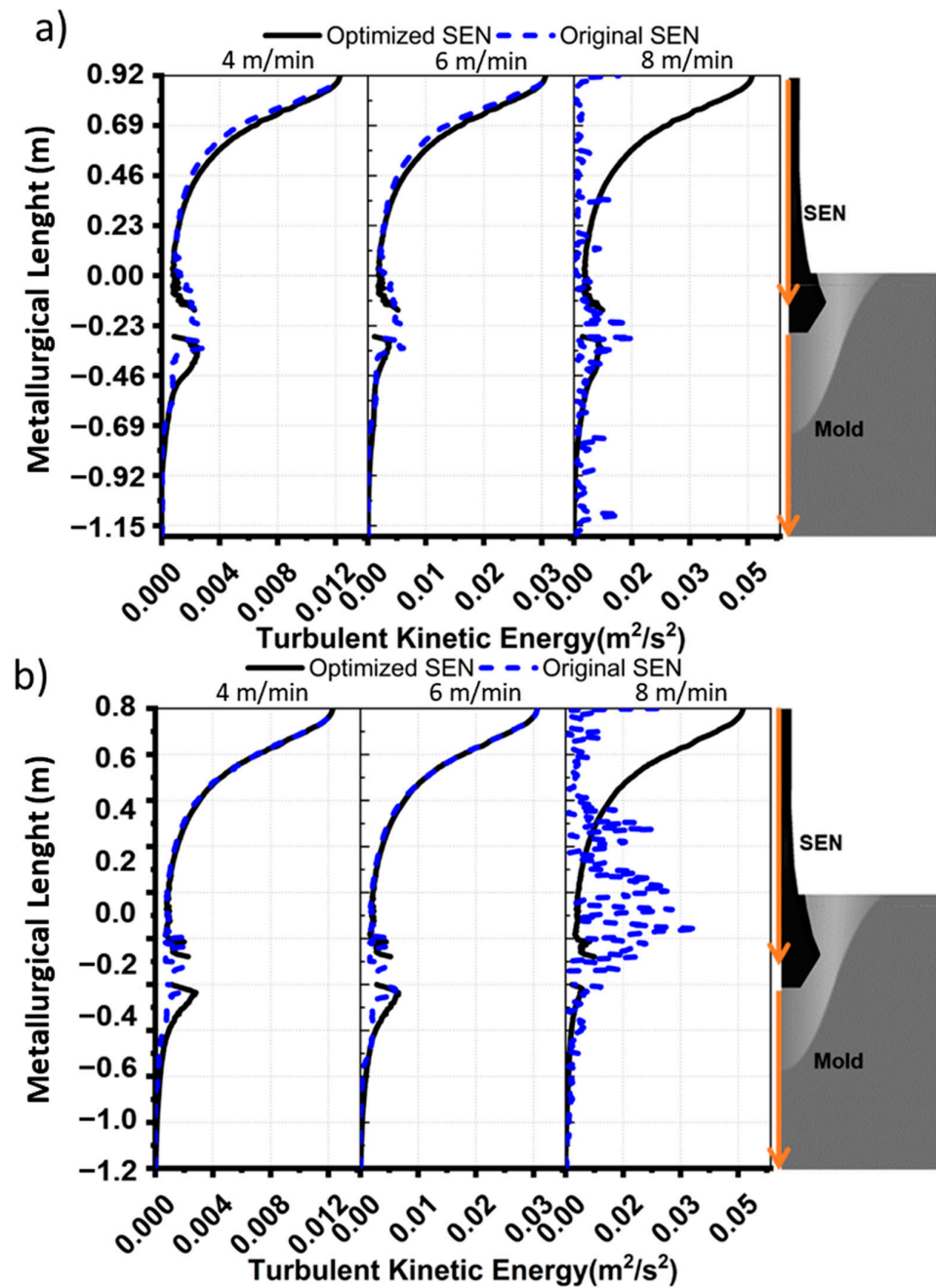


Figure 17. Effect of the internal geometry of the nozzle and the metallurgical height on the turbulent kinetic energy, measured in a vertical line drawn inside the nozzle and the mold for (a) 22 cm nozzle immersion and (b) 34 cm nozzle immersion.

Part b of Figure 17 for a 34 cm nozzle immersion depicts the turbulent kinetic energy of the fluid inside the nozzle for a casting speed that comes from a maximum of kinetic energy production. The speed decreases as it moves deeper into the nozzle, until it reaches the division of the ports, managing to increase when colliding with it and reaching very similar values for both nozzles. Let us now analyze the nozzle for a 6 m/min casting speed. It can be seen how the original nozzle has a minimal production of turbulent kinetic energy both inside the nozzle and in the mold, while the optimized nozzle comes from a production of null kinetic energy at the entrance of the nozzle, increasing until it reaches a maximum of 20 cm inside the nozzle and gradually decreasing until it reaches the tip of the division of the ports, where it reaches a maximum value in the production of turbulent kinetic energy.

If the casting speed of 8 m/min is analyzed, it is possible to observe the same behavior for the optimized nozzle. In contrast, the original nozzle presents a constant fluctuation of energy inside, while the optimized nozzle presents the expected average behavior; if the behavior of the kinetic energy inside the mold is analyzed, the optimized nozzle presents a more outstanding production of turbulent kinetic energy up to 20 cm below the tip of the nozzle for casting speeds of 4, 6, and 8 m/min, while the original nozzle at 8 m/min still shows an energy fluctuation that covers the entire region of the mold. The difference is in how the kinetic energy behaves within the two nozzles. This behavior is affected by the instability at the tip of the nozzle ports, which affects the nozzle's kinetic energy. The optimized nozzle's design allows for energy sharing between the two jets from the nozzle ports, while the original nozzle's design is based on the fluid coming from the bottom and reaching the nozzle's tip.

Regarding Figure 18 for the dissipation relationship of the turbulent kinetic energy, at 22 cm immersion of the nozzle in part (a), both nozzles similarly dissipate the energy for casting speeds of 4 and 6 m/min. However, there is a vast difference in the amount of energy dissipated when the fluid hits the tip of the port division. Accordingly, the optimized nozzle disperses a more significant amount of energy in the turbulent mold kinetics, just below the tip of the nozzle. This result is directly related to the production–dissipation relationship created by the collision of both jets in this area. Furthermore, the occurrence is related to eliminating the space left by the original nozzle. As a result, the fluid from the bottom and the upper part of the mold interact, causing continuous vortices.

After examining parts (a) and (b) at a casting speed of 8 m/min, this behavior completely changes for the original nozzle. Here, it shows a fluctuating behavior in kinetic energy dissipation inside the nozzle and the mold. Thus, inside the mold, the oscillation of the jets increases, and vortex path energy is generated between the jets. This effect resulted in a transfer movement in the recirculation in the upper part of the mold.

In contrast, the optimized nozzle presented a typical 4 and 6 m/min pattern. When analyzing subsection (b) for an immersion depth of 34 cm, the same behavior is observed for 22 cm nozzle immersion at casting speeds of 4 and 6 m/min. Even though there is a slight difference in the optimized nozzle, the difference is related to the dissipation of more kinetic energy over the tip of the port division, corresponding to the hydrostatic pressure effect on both nozzles. In the case of the optimized nozzle, the division size of the ports is 2.06 times higher than that of the original nozzle. Hence, it is less affected by hydrostatic pressure and seeks to reach dynamic equilibrium faster. Now, analyzing the kinetic energy dissipation for the 8 m/min casting speed, the same behavior is observed for the 22 cm nozzle immersion, continuing and fluctuating for the original nozzle. In contrast, the optimized nozzle maintains the demeanor obtained at lower speeds. The fluctuation in dissipation and kinetic energy production corresponds to the jet oscillation inside the mold, consequently forming the vortex path below the tip of the nozzle.

Figure 19 shows the turbulent intensity related to the fluctuating and average speeds. In parts (a) and (b) of Figure 19, this can be seen clearly for 22 and 34 cm nozzle immersion at casting speeds of 4 and 6 m/min inside both nozzles and the mold, as the fluctuating speed begins to grow.

At the same time, the instantaneous velocity of the fluid decays, with the original nozzle having a very pronounced change at the moment of the impact of the fluid with the division of the ports. This change occurs due to the fluctuating velocity increase between the neighboring fluid layers. As a result, it simultaneously destabilizes the flow in each port.

When the nozzle flow exits just below the tip of the division of the ports, the optimized nozzle instantaneously regains its velocity, suppressing vorticity and velocity fluctuations due to the kinetic energy shared between the jets and different fluid layers inside the mold. The speed analysis confirmed the original nozzle flow pattern, which had fluctuating and rising velocity, and the formation of vortex paths with a vector field of both nozzles and the same casting speeds.

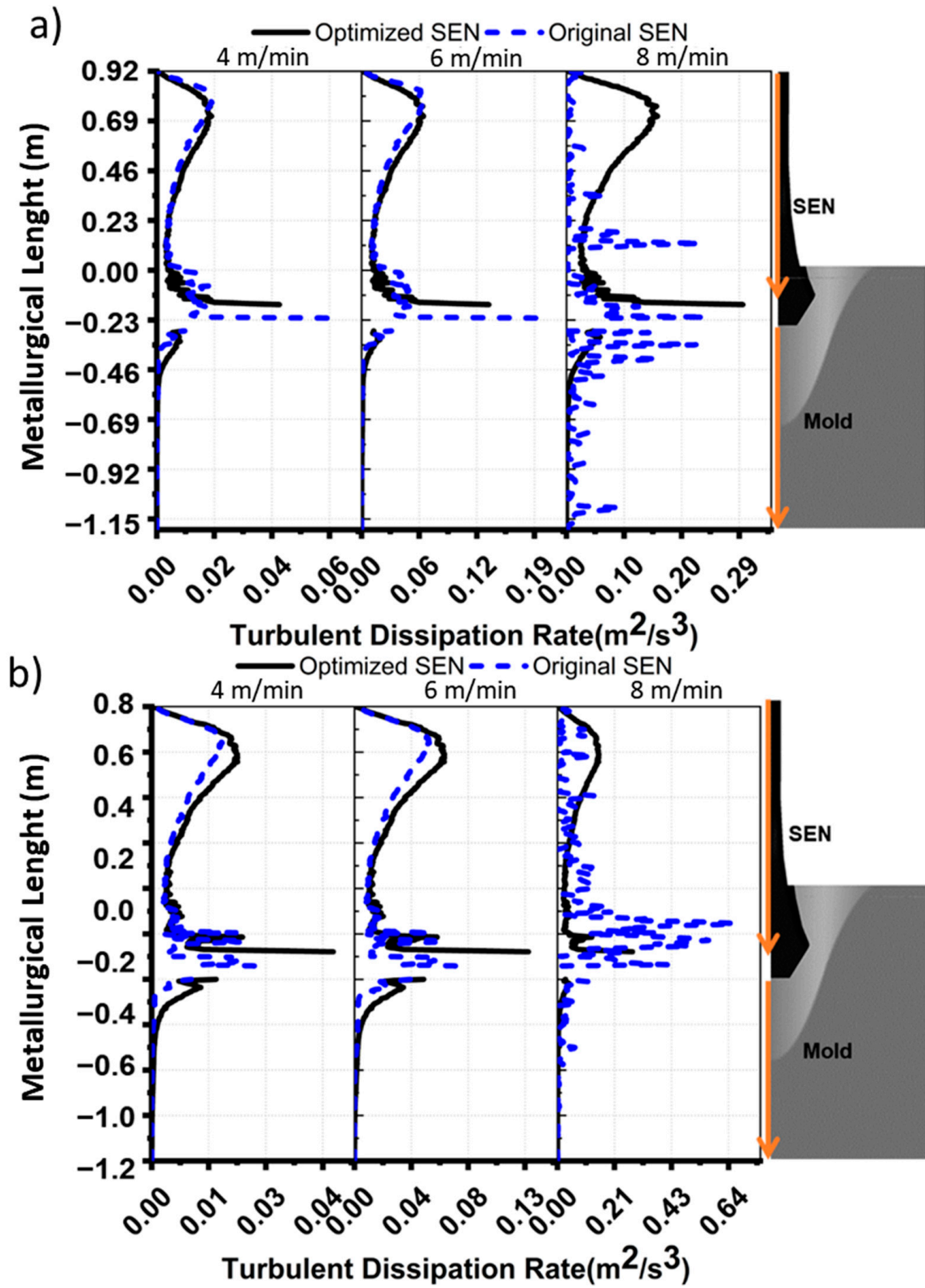


Figure 18. Effect of the internal geometry of the nozzle and the metallurgical height on the turbulent dissipation rate, measured in a vertical line drawn inside the nozzle and the mold for (a) 22 cm nozzle immersion and (b) 34 cm nozzle immersion.

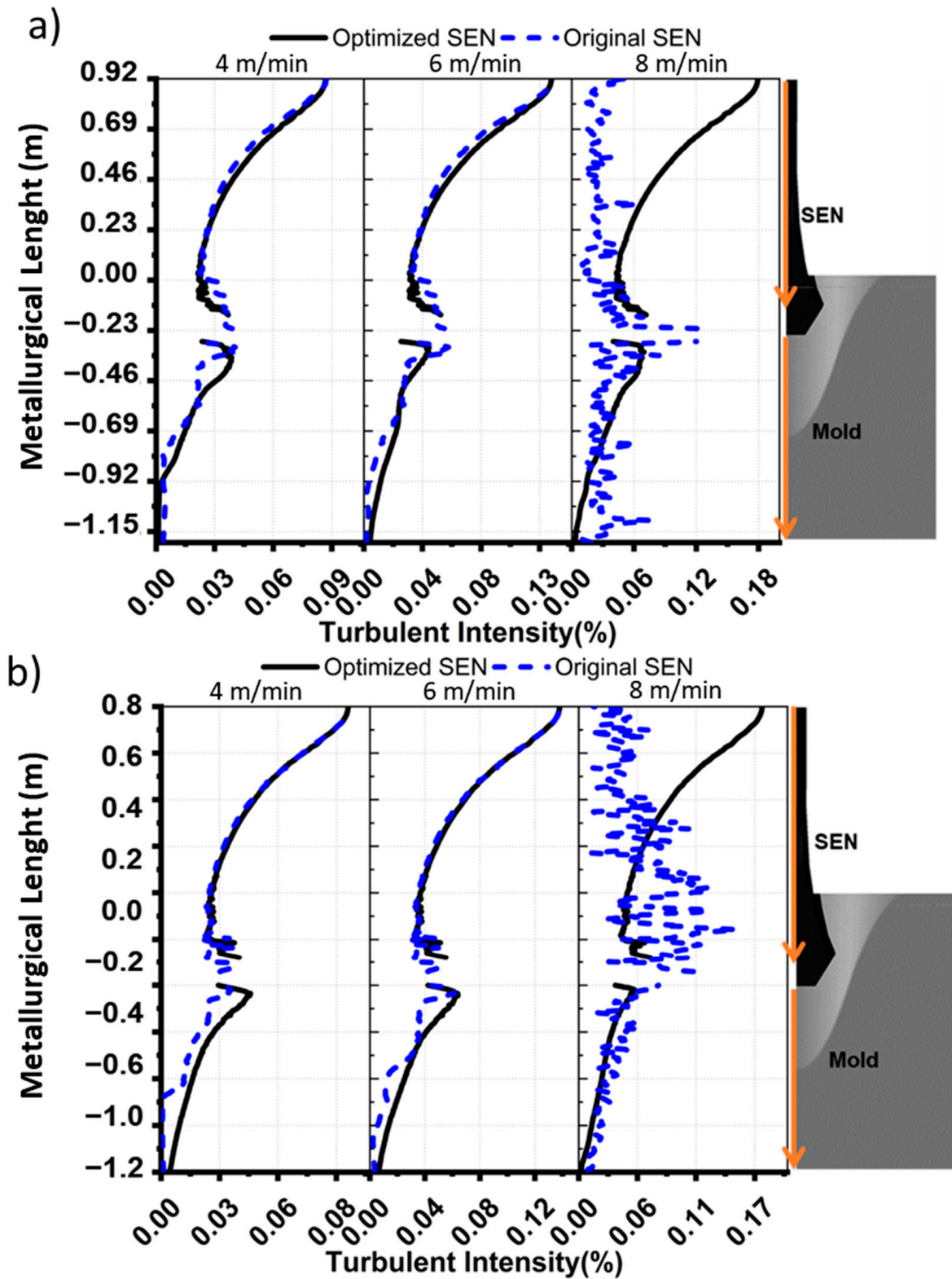


Figure 19. Effect of the internal geometry of the nozzle and the metallurgical height on the turbulent intensity, measured in a vertical line drawn inside the nozzle and the mold for (a) 22 cm nozzle immersion and (b) 34 cm nozzle immersion.

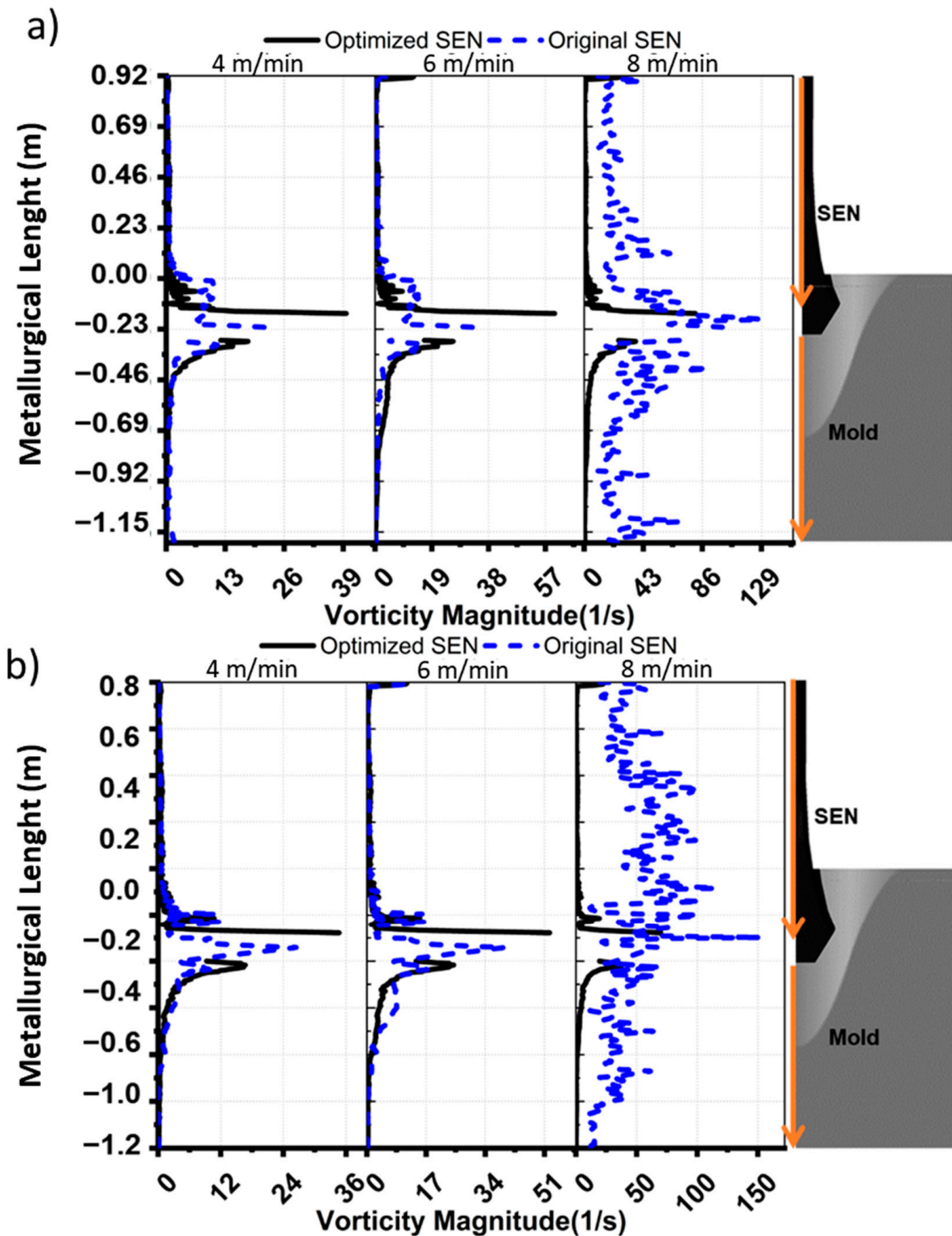


Figure 20. Effect of the internal geometry of the nozzle and the metallurgical height on the vorticity magnitude, measured in a vertical line drawn inside the nozzle and the mold for (a) 22 cm nozzle immersion and (b) 34 cm nozzle immersion.

In contrast to the 8 m/min speed for both immersion levels, the optimized nozzle maintains the same profile, unlike the original nozzle, since there is a constant exchange between the fluctuating speed and the instantaneous speed. This fluctuating behavior in the turbulent intensity increases the periodicity in forming vortices. As a result, it destabilizes

the flow inside the nozzle. Finally, we verified that the jets' dynamic distortion comes from the bifurcation inside the nozzle, as a direct consequence of the vortex path and the oscillation of the casting jets.

Finally, Figure 20 corresponds to 22 cm nozzle immersion (part (a)) and 34 cm of nozzle immersion (part (b)) for casting speeds of 4, 6, and 8 m/min. Here, casting speeds of 4 and 6 m/min, and 8 m/min, present the most noticeable vorticity changes, primarily due to the impact of the flow involving the division of the ports in the zone of the mold. In this consideration, the vortices fade due to the jets' energy from the original nozzle. In contrast, the immediate vorticity suppression in the modified nozzle is due to the jets' collision and the lack of space to develop the perturbation. At a speed of 8 m/min, entanglement occurs at the flow outlet of the original nozzle, caused by instability within the nozzle and resulting in vorticity formation inside the mold. The leading cause is the continuous oscillation of the nozzle jets inside the mold, putting the cleanliness of the cast steel at risk. As a result, the interface fluctuates, and the newly solidified steel crust experiences resistance due to continuous washing, provoking yarn break and a complete cessation of the process.

5. Conclusions

This research presented a numerical simulation to observe the fluid dynamics of the submerged nozzle internal design optimization (SEN) overflow patterns. The jet oscillations observed inside the mold originate from within the nozzle itself. Furthermore, it is possible to control the effect of ferrostatic pressure by reducing the depth of the nozzle concerning the metal surface. Therefore, the fluctuating flow in this area produces changes in the microscales. However, this action increases the internal pressure of the nozzle, which will undoubtedly affect its lifespan.

The internal nozzle area changes to accommodate the fluctuation of speed and pressure in the fluid zones above the port division. Consequently, impacting this zone creates an imbalance in the flow, leading to an oscillation of the jet within the nozzle. By optimizing the geometry of the port division, it is possible to suppress the vortex path area, reducing the dynamic distortion. As a result, the jets converge at the center of the mold, producing better control over the oscillations. At the tip of the internal nozzle bifurcation, the delicate and fragile balance of forces is disrupted by turbulent phenomena, resulting in fluctuation or intertwining of the flow delivered by each port.

The proposed modification in the internal geometry of the nozzle is considered capable of modifying the flow pattern inside the mold. The geometric changes correspond with a 106% greater elongation than the original nozzle; the change is considered 17% of an inverted trapezoidal shape. Furthermore, there was a 2.5 mm increase in the lower part of both ports to compensate for the inverted trapezoidal shape. The newly designed SEN successfully eliminated the issue of jet oscillations inside the mold by effectively preventing the intertwining of the flow. This improvement is a significant upgrade over the original design.

The optimizations performed in the division of the nozzle ports ensure stability in the jets coming from the nozzle ports and maintain interface integrity up to casting speeds of 8 m/min, thereby ensuring process safety and quality of the final casting product. In conclusion, this research demonstrates that dividing the internal nozzle geometry allows for better control of jet oscillations, improving process operability through interface fluctuation.

Author Contributions: Conceptualization, F.S.C., A.d.C.S.-N., J.A.B.-C., R.P.-B., V.H.M.-L., J.M.-L., G.B.-C., J.E.G.-H., H.A.-G. and I.E.G.; methodology, F.S.C., A.d.C.S.-N., J.A.B.-C., R.P.-B., V.H.M.-L., J.M.-L., G.B.-C., J.E.G.-H., H.A.-G. and I.E.G.; software, F.S.C., A.d.C.S.-N., H.A.-G. and I.E.G.; validation, F.S.C., A.d.C.S.-N., J.A.B.-C., R.P.-B., V.H.M.-L., J.M.-L., J.E.G.-H., H.A.-G. and I.E.G.; formal analysis, F.S.C., A.d.C.S.-N., J.A.B.-C., R.P.-B., V.H.M.-L., J.E.G.-H., H.A.-G. and I.E.G.; writing—original draft preparation, F.S.C., A.d.C.S.-N., J.A.B.-C., R.P.-B., V.H.M.-L., J.M.-L., G.B.-C., J.E.G.-H., H.A.-G. and I.E.G.; writing—review and editing, F.S.C., A.d.C.S.-N., J.M.-L., H.A.-G. and I.E.G.; project administration, G.B.-C., H.A.-G. and I.E.G.; All authors have read and agreed to the published version of the manuscript.

Funding: This research received no external funding.

Data Availability Statement: Data are contained within the article.

Acknowledgments: I.E. Garduño, H. Arcos–Gutiérrez, and J.E. García–Herrera gratefully acknowledge support from the Investigadores por México CONAHCYT program through project No. 674. J.A. Betancourt–Cantera, V.H. Mercado–Lemus, and R. Pérez–Bustamante acknowledge support from the Investigadores por México CONAHCYT program through project No. 850. A. Susunaga–Notario acknowledges support from the Investigadores por México CONAHCYT program through project No. 223. F.S. Chiwo and I.E. Garduño acknowledge support from COPOCYT Fideicomiso 23871 “Multas Electorales Convocatoria 2021–01” through the project “Optimización de Parámetros en Procesos de Moldeo por Inyección de Plásticos con Enfoque Hacia Manufactura 4.0”.

Conflicts of Interest: The authors declare no conflicts of interest.

References

1. Shen, B.Z.; Shen, H.F.; Liu, B.C. Water modelling of level fluctuation in thin slab continuous casting mould. *Ironmak. Steelmak.* **2009**, *36*, 33–38. [[CrossRef](#)]
2. Yuan, Q.; Thomas, B.G.; Vanka, S.P. Study of transient flow and particle transport in continuous steel caster molds: Part I. Fluid flow. *Met. Mater. Trans. B* **2004**, *35*, 685–702. [[CrossRef](#)]
3. Jeon, Y.J.; Sung, H.J.; Lee, S. Flow Oscillations and Meniscus Fluctuations in a Funnel-Type Water Mold Model. *Met. Mater. Trans. B* **2009**, *41*, 121–130. [[CrossRef](#)]
4. Torres-Alonso, E.; Morales, R.; García-Hernández, S.; Palafox-Ramos, J. Cyclic Turbulent Instabilities in a Thin Slab Mold. Part I: Physical Model. *Met. Mater. Trans. B* **2010**, *41*, 583–597. [[CrossRef](#)]
5. Torres-Alonso, E.; Morales, R.D.; Demedices, L.G.; Nájera, A.; Palafox-Ramos, J.; Ramirez-Lopez, P. Flow Dynamics in Thin Slab Molds Driven by Sustainable Oscillating Jets from the Feeding SEN. *ISIJ Int.* **2007**, *47*, 679–688. [[CrossRef](#)]
6. Sun, Y.-H.; Ni, Y.-J.; Wang, H.-T.; Xu, Z.-B.; Cai, K.-K. Longitudinal surface cracks of thin slabs. *Int. J. Miner. Met. Mater.* **2010**, *17*, 159–166. [[CrossRef](#)]
7. Gupta, D.; Lahiri, A.K. A water model study of the flow asymmetry inside a continuous slab casting mold. *Met. Mater. Trans. B* **1996**, *27*, 757–764. [[CrossRef](#)]
8. Zhang, X.; Chen, W.; Scheller, P.R.; Ren, Y.; Zhang, L. Mathematical Modeling of Initial Solidification and Slag Infiltration at the Meniscus of Slab Continuous Casting Mold. *JOM* **2018**, *71*, 78–87. [[CrossRef](#)]
9. Yavuz, M.M. The Effects of Electromagnetic Brake on Liquid Steel Flow in Thin Slab Caster. *Steel Res. Int.* **2011**, *82*, 809–818. [[CrossRef](#)]
10. Liu, H.; Yang, C.; Zhang, H.; Zhai, Q.; Gan, Y. Numerical Simulation of Fluid Flow and Thermal Characteristics of Thin Slab in the Funnel-Type Molds of Two Casters. *ISIJ Int.* **2011**, *51*, 392–401. [[CrossRef](#)]
11. Tian, X.-Y.; Li, B.-W.; He, J.-C. Numerical analysis of influences of casting speeds on fluid flow in funnel shape mould with new type EMBr. *Int. J. Cast Met. Res.* **2010**, *23*, 73–80. [[CrossRef](#)]
12. Li, B.; Tsukihashi, F. Effects of Electromagnetic Brake on Vortex Flows in Thin Slab Continuous Casting Mold. *ISIJ Int.* **2006**, *46*, 1833–1838. [[CrossRef](#)]
13. Garcia-Hernandez, S.; Gonzalez-Guzman, C.H.; Davila, R.M.; Barreto, J.d.J.; Gutierrez, E.; Calderon-Ramos, I. Modeling Study of EMBr Effects on the Detrimental Dynamic Distortion Phenomenon in a Funnel Thin Slab Mold. *Crystals* **2020**, *10*, 958. [[CrossRef](#)]
14. Yu, S.; Long, M.; Zhang, M.; Chen, D.; Xu, P.; Duan, H.; Yang, J. Effect of mold corner structures on the fluid flow, heat transfer and inclusion motion in slab continuous casting molds. *J. Manuf. Process.* **2021**, *68*, 1784–1802. [[CrossRef](#)]
15. Wang, C.; Liu, Z.; Li, B. Combined Effects of EMBr and SEMs on Melt Flow and Solidification in a Thin Slab Continuous Caster. *Metals* **2021**, *11*, 948. [[CrossRef](#)]
16. Moon, C.-H.; Lee, D.M.; Moon, S.-C.; Park, H.-D. Re-start Technology for Reducing Sticking-type Breakout in Thin Slab Caster. *ISIJ Int.* **2008**, *48*, 48–57. [[CrossRef](#)]
17. Vdovin, K.N.; Zlov, V.E.; Suspitsin, V.G. Deformation of the skin of a continuous-cast slab in the mold of the caster. *Metallurgist* **2009**, *53*, 572–576. [[CrossRef](#)]
18. Li, X.; Li, B.; Liu, Z.; Niu, R.; Liu, Y.; Zhao, C.; Huang, C.; Qiao, H.; Yuan, T. Large Eddy Simulation of Multi-Phase Flow and Slag Entrapment in a Continuous Casting Mold. *Metals* **2018**, *9*, 7. [[CrossRef](#)]
19. Zhao, P.; Zhou, L. Mathematical modelling of slag entrainment and entrained droplets in a continuous casting mould. *Ironmak. Steelmak.* **2019**, *46*, 886–895. [[CrossRef](#)]
20. Bielnicki, M.; Jowska, J. Physical and numerical modeling of liquid slag entrainment in mould during slabs casting. *Met. Res. Technol.* **2020**, *117*, 509. [[CrossRef](#)]
21. Torres-Alonso, E.; Morales, R.; García-Hernández, S. Cyclic Turbulent Instabilities in a Thin Slab Mold. Part II: Mathematical Model. *Met. Mater. Trans. B* **2010**, *41*, 675–690. [[CrossRef](#)]
22. Hajari, A.; Meratian, M. Surface turbulence in a physical model of a steel thin slab continuous caster. *Int. J. Miner. Met. Mater.* **2010**, *17*, 697–703. [[CrossRef](#)]

23. Saldaña-Salas, F.; Torres-Alonso, E.; Ramos-Banderas, J.; Solorio-Díaz, G.; Hernández-Bocanegra, C. Analysis of the Depth of Immersion of the Submerged Entry Nozzle on the Oscillations of the Meniscus in a Continuous Casting Mold. *Metals* **2019**, *9*, 596. [[CrossRef](#)]
24. Morales, R.D.; Palafox-Ramos, J.; Garcia-Demedices, L.; Sanchez-Perez, R. A DPIV Study of Liquid Steel Flow in a Wide Thin Slab Caster Using Four Ports Submerged Entry Nozzles. *ISIJ Int.* **2004**, *44*, 1384–1392. [[CrossRef](#)]
25. Kolahdooz, A.; Nourouzi, S.; Jooybari, M.B.; Hosseinipour, S. Experimental investigation of the effect of temperature in semisolid casting using cooling slope method. *Proc. Inst. Mech. Eng. Part E J. Process Mech. Eng.* **2016**, *230*, 316–325. [[CrossRef](#)]
26. Zhang, L.; Yang, S.; Cai, K.; Li, J.; Wan, X.; Thomas, B.G. Investigation of Fluid Flow and Steel Cleanliness in the Continuous Casting Strand. *Metall. Mater. Trans. B* **2007**, *38*, 63–83. [[CrossRef](#)]
27. Liu, Z.; Li, B.; Tsukihashi, F. Instability and Periodicity of Asymmetrical Flow in a Funnel Thin Slab Continuous Casting Mold. *ISIJ Int.* **2015**, *55*, 805–813. [[CrossRef](#)]
28. Xuan, M.; Chen, M. Optimal Design of the Submerged Entry Nozzle for Thin Slab Continuous Casting Molds. *Metals* **2021**, *11*, 1223. [[CrossRef](#)]
29. Zhang, X.; Chen, W.; Ren, Y.; Zhang, L. Mathematical Modeling on the Influence of Casting Parameters on Initial Solidification at the Meniscus of Slab Continuous Casting. *Met. Mater. Trans. B* **2019**, *50*, 1444–1460. [[CrossRef](#)]
30. Honeyands, T.; Herbertson, J. Flow dynamics in thin slab caster moulds. *Steel Res.* **1995**, *66*, 287–293. [[CrossRef](#)]
31. Zhang, L.; Wang, Y.; Zuo, X. Flow transport and inclusion motion in steel continuous-casting mold under submerged entry nozzle clogging condition. *Metall. Mater. Trans. B* **2008**, *39*, 534–550. [[CrossRef](#)]
32. Zhang, T.; Yang, J.; Jiang, P. Measurement of Molten Steel Velocity near the Surface and Modeling for Transient Fluid Flow in the Continuous Casting Mold. *Metals* **2019**, *9*, 36. [[CrossRef](#)]
33. Arcos-Gutierrez, H.; Barrera-Cardiel, G.; Barreto, J.d.J.; Garcia-Hernandez, S. Numerical Study of Internal SEN Design Effects on Jet Oscillations in a Funnel Thin Slab Caster. *ISIJ Int.* **2014**, *54*, 1304–1313. [[CrossRef](#)]
34. Liu, R.; Blazek, K.; Forman, B.; Fritz, C.; Graham, C. Effect of Submerged-Entry Nozzle (SEN) Design on Fluid Flow and Heat Transfer in a Thin-Slab Steel Caster. *Steel Res. Int.* **2019**, *90*, 1800398. [[CrossRef](#)]
35. Andersson, B. *Computational Fluid Dynamics for Engineers*; Cambridge University Press: Cambridge, UK, 2020.
36. Wilcox, D.C. *Turbulence Modeling for CFD*; DCW Industries: La Cañada, CA, USA, 2010.
37. Schlichting, H.S.; Gersten, K. *Boundary-Layer Theory*; Springer: Berlin/Heidelberg, Germany, 2018.
38. Chapters 12 and 23. In *FLUENT 6.2. User's Guide*; Fluent Inc.: Lebanon, NH, USA, 2005.
39. Heaslip, L.J.; McLean, A.; Sommerville, I.D. *Continuous Casting*; Iron and Steel Society of AIME: Warrendale, PA, USA, 1983.
40. Pope, S.B. *Turbulent Flows*; Cambridge University Press: London, UK, 2000.
41. Ramirez, O.S.D.; Torres-Alonso, E.; Banderas, J.R.; Villa, S.A.A.; Bocanegra, C.A.H.; Martínez, J.S.T. Thermal and Fluid-Dynamic Optimization of a Five Strand Asymmetric Delta Shaped Billet Caster Tundish. *Steel Res. Int.* **2018**, *89*, 1700428. [[CrossRef](#)]
42. Volpp, J. Surface tension of steel at high temperatures. *SN Appl. Sci.* **2023**, *5*, 237. [[CrossRef](#)]

Disclaimer/Publisher's Note: The statements, opinions and data contained in all publications are solely those of the individual author(s) and contributor(s) and not of MDPI and/or the editor(s). MDPI and/or the editor(s) disclaim responsibility for any injury to people or property resulting from any ideas, methods, instructions or products referred to in the content.